

Supplementary Information

Star-Shaped Pt(II) Complexes with Excellent Optical Power

Limiting Performance and Their Flexible Optical Limiters

Lai Hu, Zhiyuan Chen, Zhi Zhao, Ruiqi Chen, Senqiang Zhu*, Rui Liu*, and Hongjun Zhu

School of Chemistry and Molecular Engineering, Nanjing Tech University, Nanjing, 211816, China

E-mail: zhusenqiang1993@njtech.edu.cn (S. Zhu); rui.liu@njtech.edu.cn (R. Liu).

1. Experimental Section

1.1 General information

All starting chemicals were obtained from commercial suppliers and used as received, unless otherwise specified. Intermediates **1a–1c**, **trans-Pt(PBu₃)₂Cl₂**, **2**, and **3** were synthesized following previously reported methods.^{S1–S6} PDMS (Polydimethylsiloxane, SYLGARD 184) was obtained from Dow Corning Silicone Trading Co., Ltd. (Shanghai, China), consisting of a base gum and curing agent. Tetrahydrofuran (THF) was dried over sodium wire and distilled under a dry nitrogen atmosphere prior to use.

Nuclear magnetic resonance (NMR) spectra were recorded on a Bruker AV-400 spectrometer at 298 K. Chemical shifts are referenced in ppm relative to the signals of residual non-deuterated solvents (CDCl₃: $\delta_{\text{H}} = 7.26$ ppm and $\delta_{\text{C}} = 77.0$ ppm). Matrix-assisted laser desorption/ionization time-of-flight (MALDI-TOF) mass spectra were obtained using a Bruker autoflex maX MALDI-TOF mass spectrometer. X-ray diffraction data were collected on a Bruker D8-Venture, Bruker APEX-II CCD, or Bruker PHOTON III detector, using Mo-K α ($\lambda = 0.71073$ Å) or Cu-K α ($\lambda = 1.54184$ Å) radiation. The structures were solved with the SHELXT structure solution program

using Intrinsic Phasing and refined with the SHELXL refinement package, employing Least Squares minimization in OLEX2 program. The X-ray crystallographic data for **Pt-1b**, **Pt-2b**, **Pt-1c**, and **Pt-2c** have been deposited at the Cambridge Crystallographic Data Centre (CCDC) under the deposition number CCDC **2288730**, **2288731**, **2213945**, and **2288732**, respectively. UV-vis spectra were measured using a TU-1900 UV spectrophotometer. Photoluminescence (PL) spectra, emission lifetimes and absolute phosphorescence quantum yields were measured on an Edinburgh FLS1000 fluorescence spectrometer. Nanosecond transient absorption (ns-TA) spectra were detected on an LP980 laser flash photolysis spectrometer (Edinburgh Instruments, U.K.). The excitation source was the third harmonic output (355 nm) of a Nd: YAG laser (Continuum Surelite, pulse width: 4.0 ns, repetition rate: 1.0 Hz). The solutions were purged with nitrogen for 30 min before measurement. Thermogravimetric analysis (TGA) was performed on a NETZSCH STA 449 F5 with a heating rate of 10 °C min⁻¹ under a nitrogen atmosphere. Mechanical tensile tests were carried out using an INSTRON 3343 universal testing machine. Scanning electron microscopy (SEM) were performed on a Hitachi Regulus 8100 scanning electron microscope.

1.2 Computational details

All calculations were performed using the Gaussian 09 software package.^{S7} Density functional theory (DFT) calculations were carried out with the popular B3LYP functional. The effective core potentials with a LanL2DZ basis set were employed for the Pt atoms, while the 6-31G(d, p) and 6-31G(d) basis sets were used for other atoms for the ground-state and excited-state calculation. All the alkyl groups in the Pt(II) complexes were replaced with the methyl groups to simplify the calculation process. The geometries of the ground-state and triplet excited-state structures were fully optimized in gas phase without any structural constraints. The frequency calculations were performed at the same level of theory to confirm that each configuration was a stable state. Time-dependent DFT (TD-DFT) calculations were performed to calculate the vertical excitation energies. Natural transition orbitals (NTOs) were calculated by

TD-DFT calculations at the optimized triplet excited-state geometries obtained by the unrestricted B3LYP (UB3LYP) method. The orbital composition were analyzed by Multiwfn package and the orbitals were visualized by VMD program (the isovalue was set as 0.02).^{S8}

1.3 Z-scan and optical power limiting measurements

The nonlinear optical properties of samples at 532 nm were evaluated by using the standard Z-scan technique^{S9} in the open mode with a Q-switched Nd: YAG laser (Continuum Surelite, pulse width: 4.0 ns, repetition rate: 10 Hz). The sample was loaded onto the platform, which was driven by a stepper motor and moved accurately over a distance of ± 30 mm from the laser focal point ($Z = 0$) along with the optical z-axis. The spatial and temporal profiles of the laser pulses presented an approximately Gaussian distribution. The laser beam was split into two parts: one was collected by a reference detector to monitor energy fluctuations, while the other was focused onto the sample using a lens to measure the transmittance as the sample was scanned along the Z-axis, varying the laser intensity. The concentrations of **Pt-1a–Pt-2c** were adjusted to 1×10^{-3} mol L⁻¹ and measured in a quartz cuvette with 2 mm path length. For PDMS film samples, the 2 mm thick films were directly placed on the platform for measurement.

The laser source used for optical power limiting measurements was the same as that used for the open-aperture Z-scan technique and the samples were placed at the focus position in the Z-scan system.

The nonlinear fitting of Z-scan curves

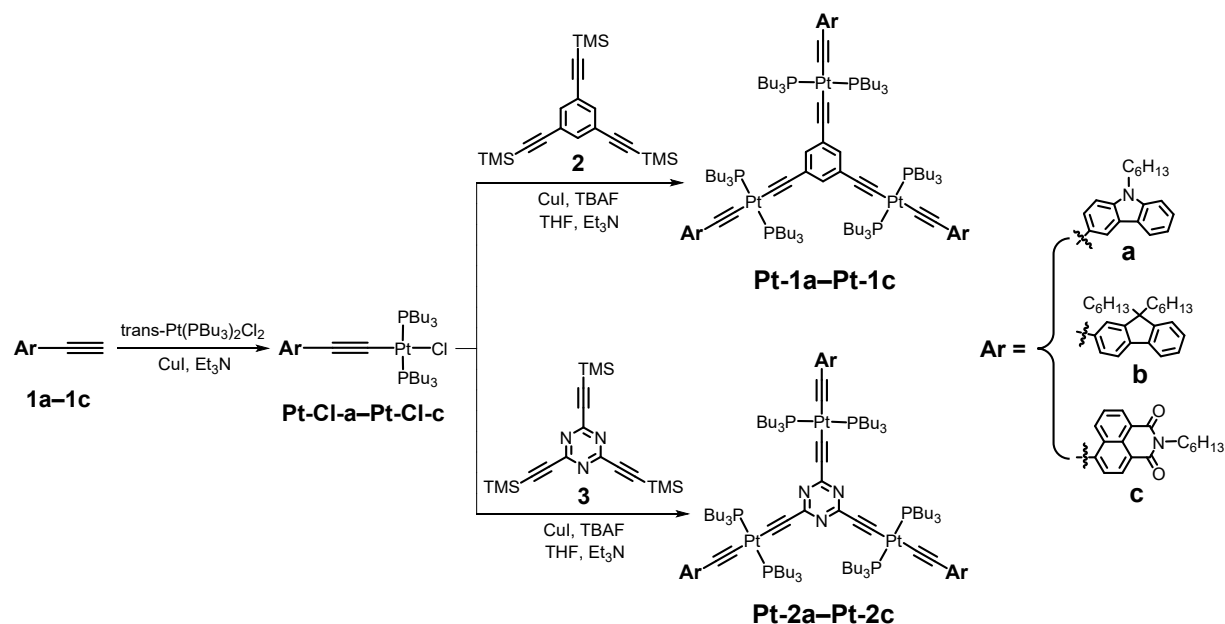
The open-aperture Z-scan curves were fitted using the transmittance equation for a third-order nonlinear process.^{S10,S11}

$$T(z, s = 1) = \sum_{m=0}^{\infty} \frac{[-q_0(z, 0)]^m}{(m+1)^{3/2}} \approx 1 - \frac{\beta_{\text{eff}} I_0 L_{\text{eff}}}{2\sqrt{2}(1 + z^2/z_0^2)} \quad (m \in \mathbb{N})$$

Where T is the normalized transmittance, β_{eff} is the effective nonlinear absorption coefficient, I_0 is the input intensity at the focal point ($z = 0$), and z represents the sample position. The effective thickness L_{eff} of the sample is given by $L_{\text{eff}} = [1 - \exp(-\alpha_0 l)]/\alpha_0$ (where l is the sample thickness), $\alpha_0 = (-\ln T_0)/l$, α_0 is the linear absorption coefficient at

the given wavelength, T_0 is the linear transmittance. $z_0 = kw_0^2/2$, z_0 is the Rayleigh diffraction length. w_0 is the beam waist at the focal point ($z = 0$). $k = 2\pi/\lambda$, where k is the wave vector and λ is the laser wavelength.

1.4 Synthesis procedures



Scheme S1. The synthetic routes for **Pt-1a-Pt-2c**.

General synthetic procedure for precursors **Pt-Cl-a-Pt-Cl-c**

Compounds **1a-1c** (5 mmol), $\text{trans-Pt(PBu}_3)_2\text{Cl}_2$ (6 mmol), and CuI (0.25 mmol) were added to a degassed THF/ Et_3N solution (50 mL, 1:1, v/v). The resulting mixture was allowed to stir at 50 °C for 12 h under a nitrogen atmosphere. After solvent removal, the residue was extracted with ethyl acetate (EA) and washed with water. The organic layer was dried over anhydrous MgSO_4 , and the solvent was evaporated under reduced pressure. The crude product was purified by column chromatography on silica gel using petroleum ether/dichloromethane (PE/DCM) as the eluent to afford the desired compound.

Pt-Cl-a: pale yellow oil (yield: 85%). $^1\text{H NMR}$ (400 MHz, CDCl_3): δ 8.03 – 7.97 (m, 2H), 7.44 (t, $J = 7.6$ Hz, 1H), 7.37 (d, $J = 8.1$ Hz, 2H), 7.26 – 7.17 (m, 2H), 4.25 (t, $J =$

7.2 Hz, 2H), 2.07 (dt, $J = 8.1, 3.9$ Hz, 12H), 1.85 (p, $J = 7.3$ Hz, 2H), 1.61 (dt, $J = 7.0, 3.6$ Hz, 12H), 1.48 (q, $J = 7.3$ Hz, 12H), 1.38 – 1.26 (m, 6H), 0.95 (t, $J = 7.2$ Hz, 18H), 0.86 (t, $J = 6.9$ Hz, 3H).

Pt-Cl-b: pale yellow oil (yield: 77%). ^1H NMR (400 MHz, CDCl_3): δ 7.64 – 7.60 (m, 1H), 7.53 (d, $J = 8.2$ Hz, 1H), 7.33 – 7.27 (m, 2H), 7.25 – 7.19 (m, 3H), 2.06 (dt, $J = 7.9, 3.8$ Hz, 12H), 1.90 (td, $J = 10.6, 5.5$ Hz, 4H), 1.67 – 1.54 (m, 12H), 1.46 (q, $J = 7.3$ Hz, 12H), 1.14 – 0.98 (m, 12H), 0.94 (t, $J = 7.3$ Hz, 8H), 0.76 (t, $J = 7.2$ Hz, 6H), 0.61 (dq, $J = 13.3, 6.5$ Hz, 4H).

Pt-Cl-c: yellow solid (yield: 71%). ^1H NMR (400 MHz, CDCl_3): δ 8.72 (d, $J = 8.2$ Hz, 1H), 8.57 (d, $J = 6.4$ Hz, 1H), 8.44 (d, $J = 7.7$ Hz, 1H), 7.67 (t, $J = 7.8$ Hz, 1H), 7.58 (d, $J = 7.7$ Hz, 1H), 4.19 – 4.10 (m, 2H), 2.01 (dt, $J = 7.7, 3.7$ Hz, 12H), 1.71 (p, $J = 7.5$ Hz, 2H), 1.66 – 1.53 (m, 12H), 1.46 – 1.30 (m, 18H), 0.90 (t, $J = 7.3$ Hz, 21H).

General synthetic procedure for complexes Pt-1a–Pt-1c

Precursors **Pt-Cl-a–Pt-Cl-c** (3.60 mmol), compound **2** (1 mmol) and CuI (0.10 mmol) were added to a degassed THF/ Et_3N solution (30 mL, 1:1 v/v). The mixture was stirred at room temperature for 30 min under a nitrogen atmosphere. Then TBAF (5 mL, 1 M in THF) was slowly injected into the mixture. The resulting mixture was stirred at 50 °C for an additional 24 h. After solvent removal, the residue was extracted with EA and washed with water. The organic layer was dried over anhydrous MgSO_4 , and the solvent was evaporated under reduced pressure. The crude product was purified by column chromatography on silica gel using PE/DCM as the eluent. The product was further purified by recrystallization from a DCM/EtOH mixture.

Pt-1a: pale yellow powder (yield: 82%). ^1H NMR (400 MHz, CDCl_3): δ 8.04 – 8.00 (m, 6H), 7.42 (d, $J = 7.9$ Hz, 6H), 7.36 (d, $J = 8.1$ Hz, 3H), 7.21 (dd, $J = 14.9, 7.4$ Hz, 6H), 7.01 (s, 3H), 4.25 (t, $J = 7.2$ Hz, 6H), 2.19 (dt, $J = 7.8, 3.9$ Hz, 36H), 1.85 (p, $J = 7.2$ Hz, 6H), 1.67 – 1.65 (m, 36H), 1.48 (q, $J = 7.3$ Hz, 36H), 1.38 – 1.27 (m, 18H), 0.96 (t, $J = 7.3$ Hz, 54H), 0.87 (t, $J = 6.9$ Hz, 9H). ^{13}C NMR (101 MHz, CDCl_3): δ

140.80, 138.53, 130.34, 129.18, 128.31, 125.46, 122.93, 122.75, 122.70, 120.32, 119.93, 118.64, 108.84, 108.73, 108.24, 43.24, 31.74, 29.11, 27.12, 26.59, 24.68, 24.61, 24.54, 24.26, 24.09, 23.92, 22.70, 14.15, 14.08. ^{31}P NMR (161.9 MHz, CDCl_3): δ 3.15 (s, ^{195}Pt satellites, $^1J_{\text{Pt-P}} = 2378.2$ Hz). HRMS (MALDI-TOF-MS): m/z calcd for $\text{C}_{144}\text{H}_{226}\text{N}_3\text{P}_6\text{Pt}_3$ $[\text{M}+\text{H}]^+$ 2768.5146, found 2768.0810.

Pt-1b: pale yellow powder (yield: 85%). ^1H NMR (400 MHz, CDCl_3): δ 7.62 (d, $J = 7.1$ Hz, 3H), 7.52 (d, $J = 8.3$ Hz, 3H), 7.29 (d, $J = 6.2$ Hz, 9H), 7.23 (d, $J = 9.7$ Hz, 6H), 6.99 (s, 3H), 2.17 (dt, $J = 7.9, 3.8$ Hz, 36H), 1.96 – 1.84 (m, 12H), 1.64 – 1.61 (m, 36H), 1.46 (dt, $J = 14.5, 7.3$ Hz, 36H), 1.14 – 1.02 (m, 36H), 0.94 (t, $J = 7.3$ Hz, 54H), 0.76 (t, $J = 7.2$ Hz, 18H), 0.61 (dq, $J = 13.3, 6.5$ Hz, 12H). ^{13}C NMR (101 MHz, CDCl_3): δ 150.70, 150.23, 141.30, 138.11, 130.19, 129.69, 128.13, 127.60, 126.60, 126.35, 125.29, 122.67, 119.28, 119.07, 110.48, 54.77, 40.62, 31.57, 29.81, 26.44, 24.52, 24.46, 24.39, 24.12, 23.95, 23.78, 23.70, 22.65, 14.01, 13.91. ^{31}P NMR (161.9 MHz, CDCl_3): δ 3.14 (s, ^{195}Pt satellites, $^1J_{\text{Pt-P}} = 2366.8$ Hz). HRMS (MALDI-TOF-MS): m/z calcd for $\text{C}_{165}\text{H}_{265}\text{P}_6\text{Pt}_3$ $[\text{M}+\text{H}]^+$ 3017.8106, found 3017.1540.

Pt-1c: yellow powder (yield: 77%). ^1H NMR (400 MHz, CDCl_3): δ 8.79 (d, $J = 9.2$ Hz, 3H), 8.57 (d, $J = 7.2$ Hz, 3H), 8.45 (d, $J = 7.7$ Hz, 3H), 7.67 (t, $J = 7.8$ Hz, 3H), 7.61 (d, $J = 7.8$ Hz, 3H), 7.03 (s, 3H), 4.16 (t, $J = 7.3$ Hz, 6H), 2.13 (dt, $J = 7.7, 3.7$ Hz, 36H), 1.75 – 1.70 (m, 6H), 1.63 (d, $J = 3.6$ Hz, 36H), 1.45 – 1.34 (m, 54H), 0.91 (t, $J = 7.3$ Hz, 63H). ^{13}C NMR (101 MHz, CDCl_3): δ 164.57, 164.28, 139.26, 134.03, 133.49, 132.17, 131.14, 131.00, 130.36, 128.53, 125.84, 122.84, 118.31, 114.06, 109.53, 108.14, 40.39, 31.60, 29.70, 28.13, 26.84, 26.50, 24.45, 24.39, 24.32, 24.13, 23.96, 22.58, 14.07, 13.88. ^{31}P NMR (161.9 MHz, CDCl_3): δ 4.20 (s, ^{195}Pt satellites, $^1J_{\text{Pt-P}} = 2340.9$ Hz). HRMS (MALDI-TOF-MS): m/z calcd for $\text{C}_{144}\text{H}_{220}\text{N}_3\text{O}_6\text{P}_6\text{Pt}_3$ $[\text{M}+\text{H}]^+$ 2858.4372, found 2858.0450.

General synthetic procedure for complexes Pt-2a–Pt-2c

Precursors **Pt-Cl-a-Pt-Cl-c** (3.60 mmol), compound **3** (1 mmol) and CuI (0.10 mmol) were added to a degassed THF/Et₃N solution (30 mL, 1:1 v/v). The mixture was stirred at 0 °C for 30 min under a nitrogen atmosphere. Then TBAF (5 mL, 1 M in THF) was slowly injected into the mixture. The resulting mixture was stirred at room temperature for an additional 24 h. After solvent removal, the residue was extracted with EA and washed with water. The organic layer was dried over anhydrous MgSO₄, and the solvent was evaporated under reduced pressure. The crude product was purified by column chromatography on silica gel using PE/DCM as the eluent. The product was further purified by recrystallization from a DCM/EtOH mixture.

Pt-2a: pale yellow powder (yield: 78%). ¹H NMR (400 MHz, CDCl₃): δ 8.02 (d, *J* = 6.3 Hz, 6H), 7.46 – 7.41 (m, 6H), 7.37 (d, *J* = 8.1 Hz, 3H), 7.26 (d, *J* = 8.5 Hz, 3H), 7.21 (t, *J* = 7.3 Hz, 3H), 4.26 (t, *J* = 7.2 Hz, 6H), 2.19 (dt, *J* = 7.7, 3.8 Hz, 36H), 1.86 (p, *J* = 6.3 Hz, 6H), 1.66 – 1.63 (m, 36H), 1.49 (q, *J* = 7.3 Hz, 36H), 1.39 – 1.27 (m, 18H), 0.96 (t, *J* = 7.3 Hz, 54H), 0.87 (t, *J* = 7.0 Hz, 9H). ¹³C NMR (101 MHz, CDCl₃): δ 160.46, 140.80, 138.56, 129.05, 125.51, 122.86, 122.74, 122.59, 120.32, 119.73, 118.68, 110.14, 108.73, 108.27, 43.23, 31.72, 29.09, 27.10, 26.58, 24.62, 24.55, 24.48, 24.33, 24.16, 23.99, 22.68, 14.13, 14.04. ³¹P NMR (161.9 MHz, CDCl₃): δ 3.40 (s, ¹⁹⁵Pt satellites, ¹*J*_{Pt-P} = 2345.7 Hz). HRMS (MALDI-TOF-MS): *m/z* calcd for C₁₄₁H₂₂₃N₃P₆Pt₃ [M+H]⁺ 2771.5004, found 2771.8134.

Pt-2b: pale yellow powder (yield: 75%). ¹H NMR (400 MHz, CDCl₃): δ 7.62 (d, *J* = 7.1 Hz, 3H), 7.53 (d, *J* = 8.3 Hz, 3H), 7.30 – 7.27 (m, 6H), 7.24 – 7.22 (m, 9H), 2.16 (dt, *J* = 7.8, 3.8 Hz, 36H), 1.89 (tq, *J* = 14.6, 7.1, 6.0 Hz, 12H), 1.61 (dt, *J* = 7.5, 3.6 Hz, 36H), 1.50 – 1.41 (m, 36H), 1.14 – 1.03 (m, 36H), 0.93 (t, *J* = 7.3 Hz, 54H), 0.76 (t, *J* = 7.2 Hz, 18H), 0.62 (dq, *J* = 13.3, 6.5 Hz, 12H). ¹³C NMR (101 MHz, CDCl₃): δ 160.35, 150.72, 150.27, 141.22, 138.23, 129.55, 127.39, 126.62, 126.41, 125.24, 122.69, 119.31, 119.11, 110.80, 110.02, 54.76, 40.56, 31.55, 29.80, 26.43, 24.47, 24.40, 24.33, 24.17, 24.00, 23.83, 23.71, 22.63, 14.00, 13.88. ³¹P NMR (161.9 MHz, CDCl₃):

δ 3.36 (s, ^{195}Pt satellites, $^1J_{\text{Pt-P}} = 2334.4$ Hz). HRMS (MALDI-TOF-MS): m/z calcd for $\text{C}_{162}\text{H}_{262}\text{N}_3\text{P}_6\text{Pt}_3$ $[\text{M}+\text{H}]^+$ 3020.7963, found 3021.0667.

Pt-2c: yellow powder (yield: 73%). ^1H NMR (400 MHz, CDCl_3): δ 8.76 (d, $J = 9.2$ Hz, 3H), 8.57 (d, $J = 6.9$ Hz, 3H), 8.45 (d, $J = 7.7$ Hz, 3H), 7.66 (t, $J = 7.8$ Hz, 3H), 7.59 (d, $J = 7.7$ Hz, 3H), 4.16 (t, $J = 7.3$ Hz, 6H), 2.11 (dt, $J = 7.7, 3.7$ Hz, 36H), 1.78 – 1.60 (m, 42H), 1.46 – 1.31 (m, 54H), 0.91 (t, $J = 7.3$ Hz, 63H). ^{13}C NMR (101 MHz, CDCl_3): δ 164.52, 164.23, 160.21, 133.67, 133.34, 132.08, 131.12, 128.55, 128.50, 125.94, 122.86, 118.53, 114.05, 110.85, 108.26, 40.39, 31.59, 31.43, 30.19, 29.69, 28.13, 26.83, 26.55, 24.43, 24.36, 24.29, 24.26, 24.09, 22.58, 14.07, 13.87. ^{31}P NMR (161.9 MHz, CDCl_3): δ 4.19 (s, ^{195}Pt satellites, $^1J_{\text{Pt-P}} = 2313.3$ Hz). HRMS (MALDI-TOF-MS): m/z calcd for $\text{C}_{141}\text{H}_{217}\text{N}_6\text{O}_6\text{P}_6\text{Pt}_3$ $[\text{M}+\text{H}]^+$ 2861.4229, found 2862.2185.

1.5 Preparation of Pt-2b@PDMS films

Pt-2b@PDMS films were prepared following the reported methods.^{S12} In brief, PDMS base gum (10 g) and curing agent (1 g) were mixed, and a specific concentration of **Pt-2b** in CH_2Cl_2 was added under stirring. The mixture was stirred for 1 h at room temperature to evaporate excess CH_2Cl_2 , resulting in a homogeneous solution. Subsequently, the solution was poured into glass substrates (diameter: 40 mm) and allowed to place in air for 30 min. The substrates were then placed in a vacuum oven at 80 °C for another 5 h. Finally, the flexible and transparent **Pt-2b@PDMS** films were obtained by peeling off. Blank PDMS and **C₆₀@PDMS** films were prepared using the same procedure. The thickness of each film measured with a vernier caliper is approximately 2 mm.

2. Structural Characterization

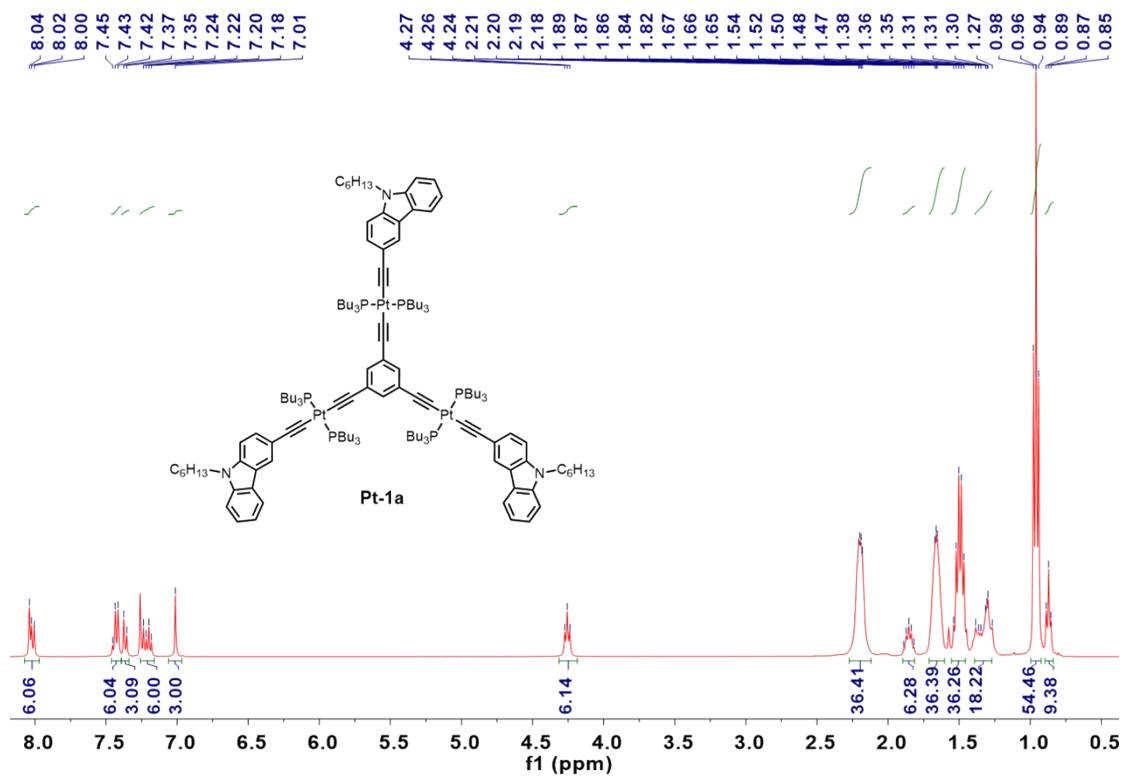


Figure S1. ¹H NMR spectrum (400 MHz, CDCl₃, 298 K) of Pt-1a.

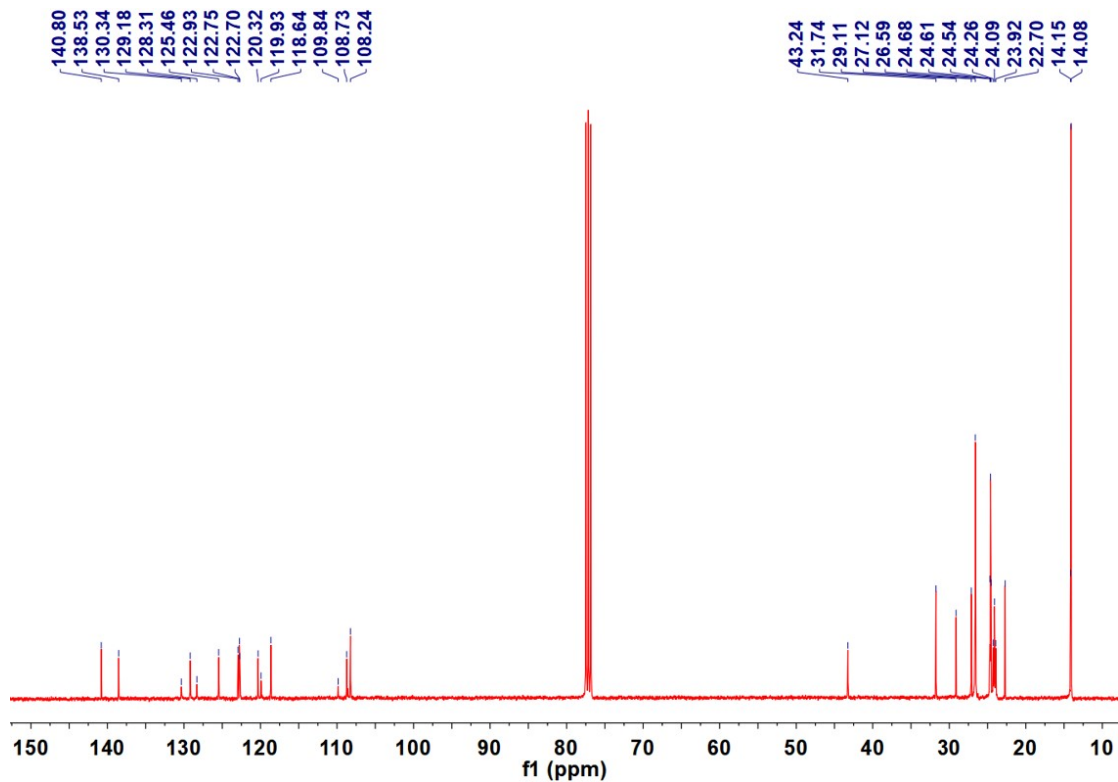


Figure S2. ¹³C NMR spectrum (101 MHz, CDCl₃, 298 K) of Pt-1a.

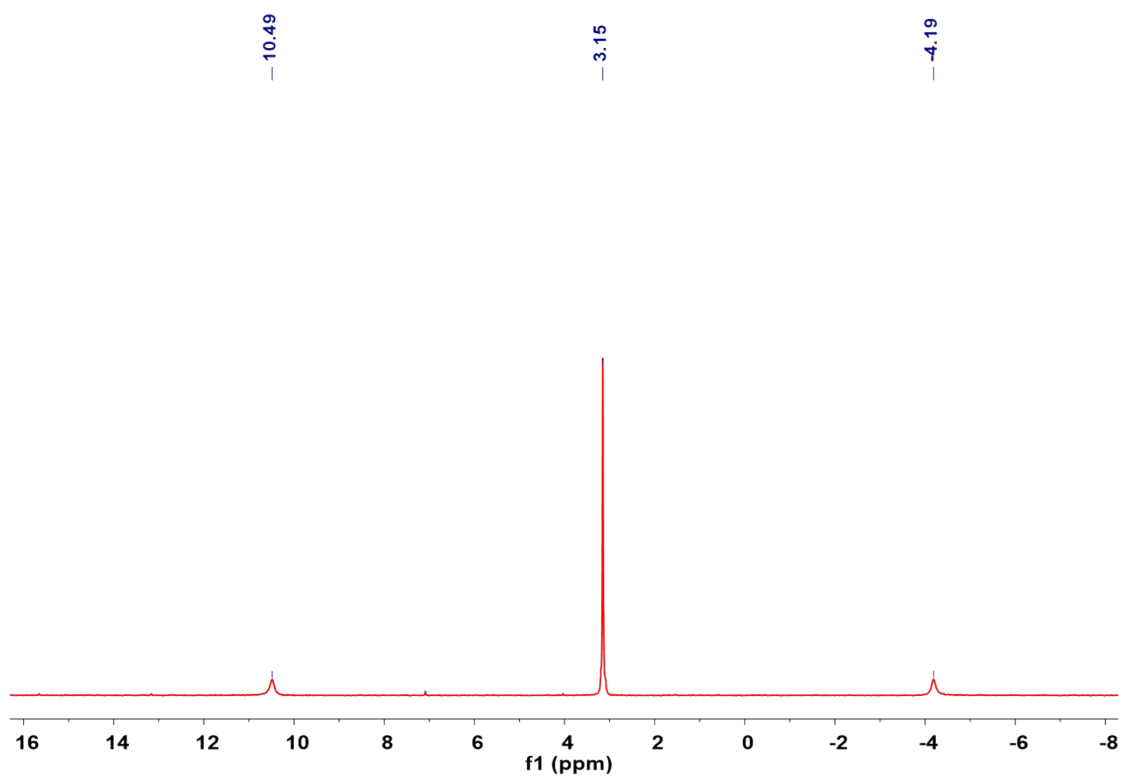


Figure S3. $^{31}\text{P}\{^1\text{H}\}$ NMR spectrum (162 MHz, CDCl_3 , 298 K) of Pt-1a.

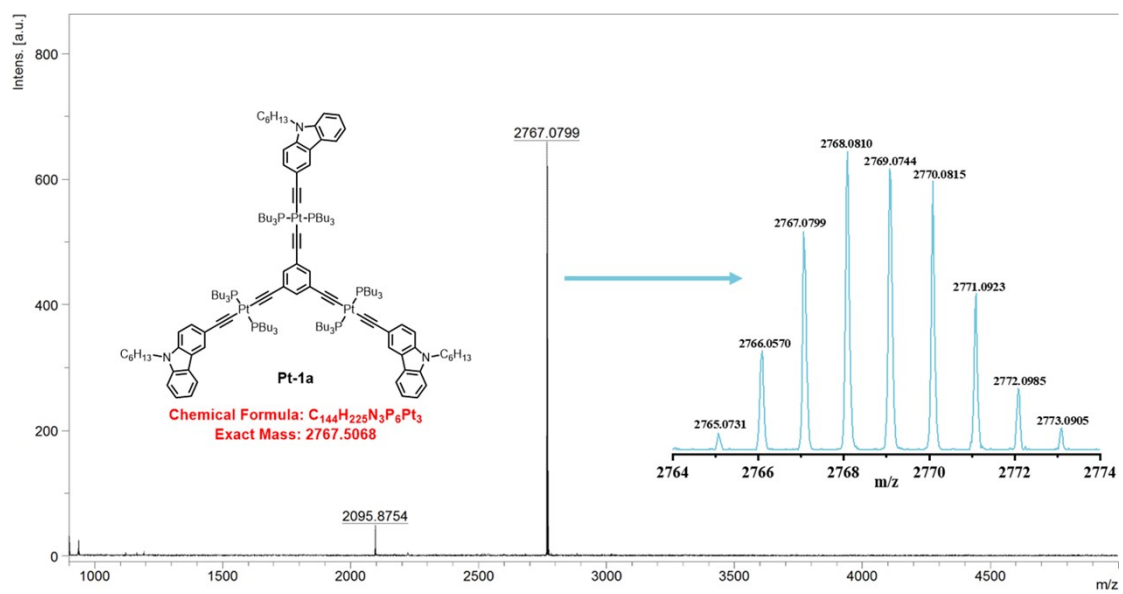


Figure S4. MALDI-TOF-MS spectrum of Pt-1a.

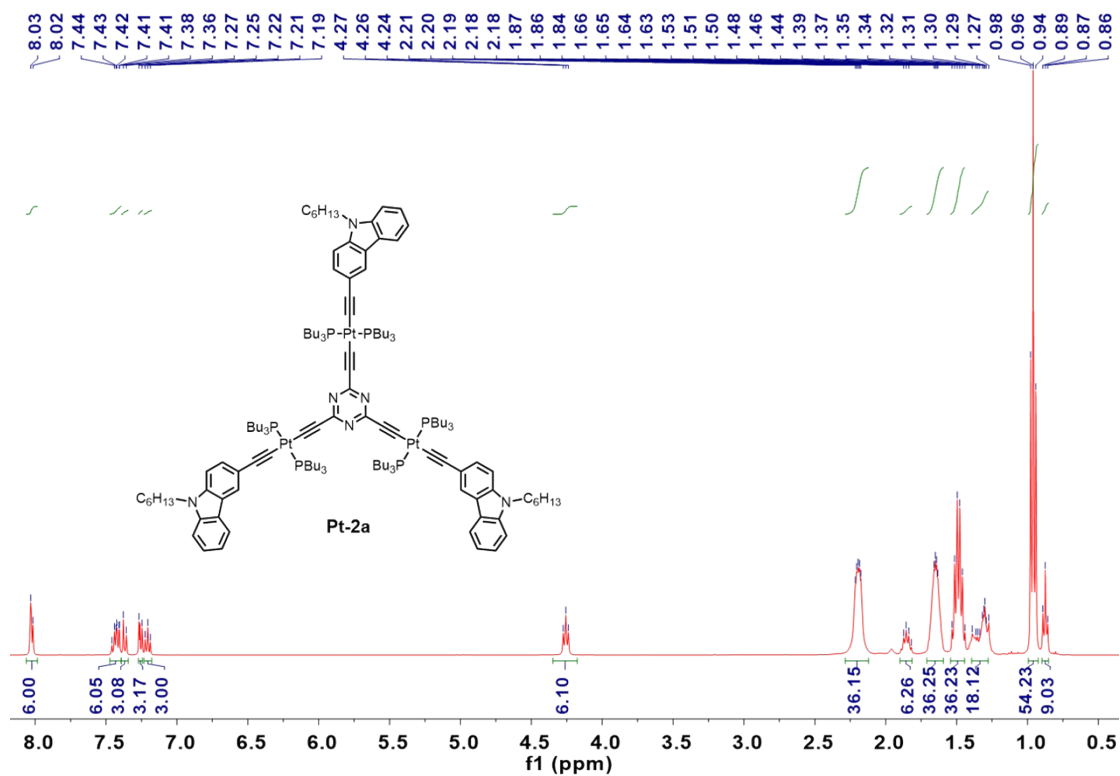


Figure S5. ¹H NMR spectrum (400 MHz, CDCl₃, 298 K) of Pt-2a.

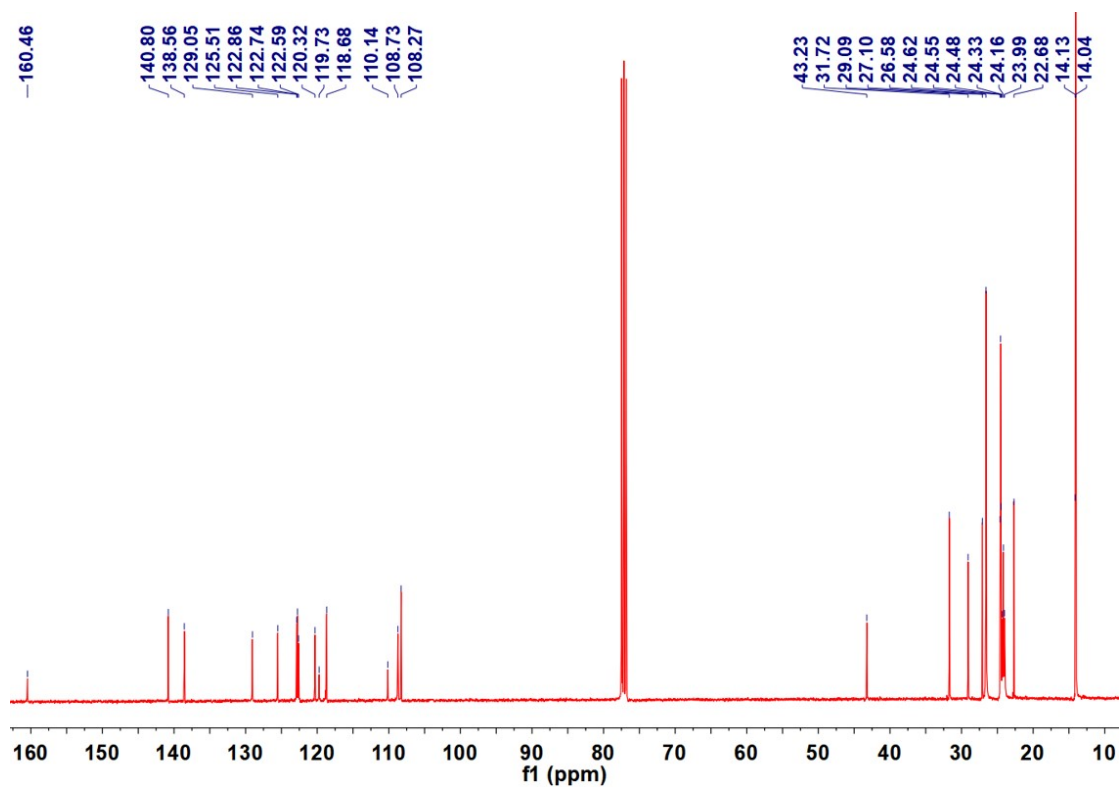


Figure S6. ¹³C NMR spectrum (101 MHz, CDCl₃, 298 K) of Pt-2a.

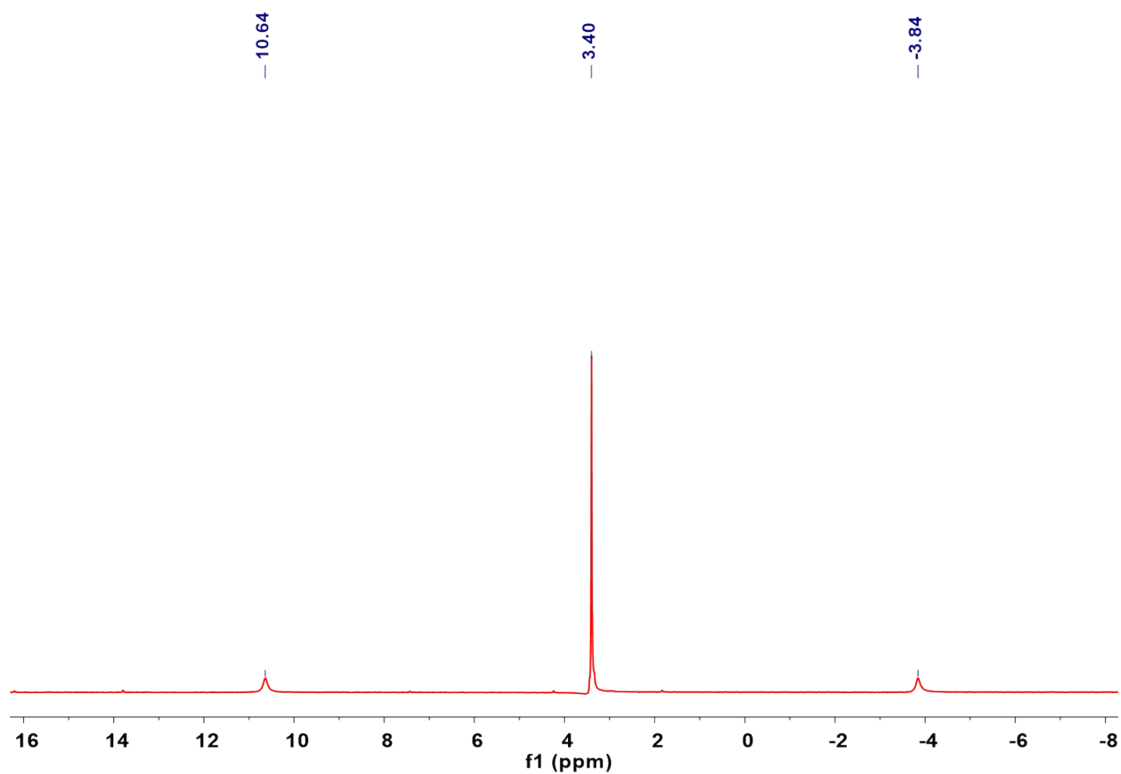


Figure S7. $^{31}\text{P}\{^1\text{H}\}$ NMR spectrum (162 MHz, CDCl_3 , 298 K) of Pt-2a.

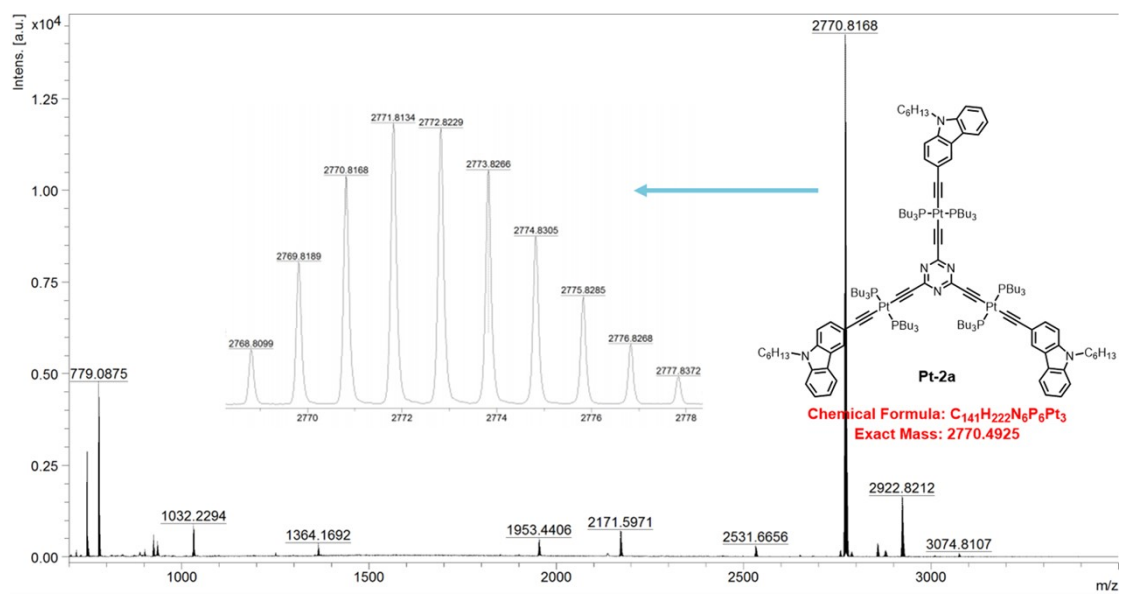


Figure S8. MALDI-TOF-MS spectrum of Pt-2a.

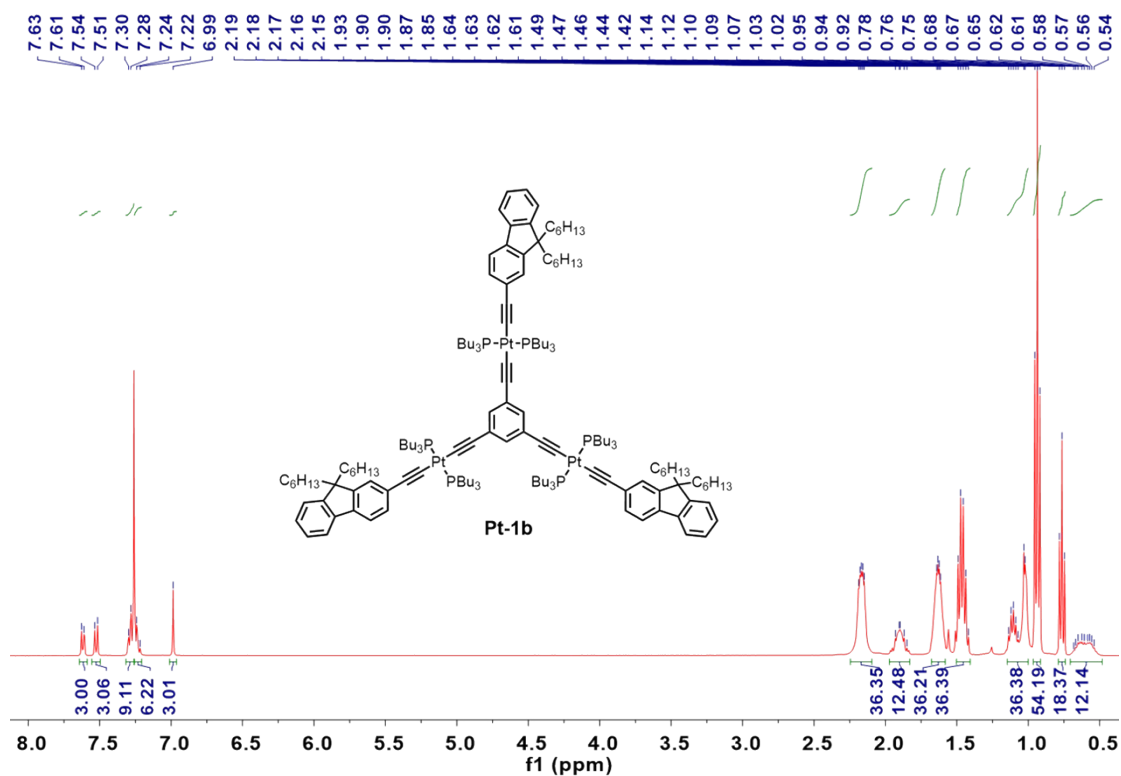


Figure S9. ¹H NMR spectrum (400 MHz, CDCl₃, 298 K) of Pt-1b.

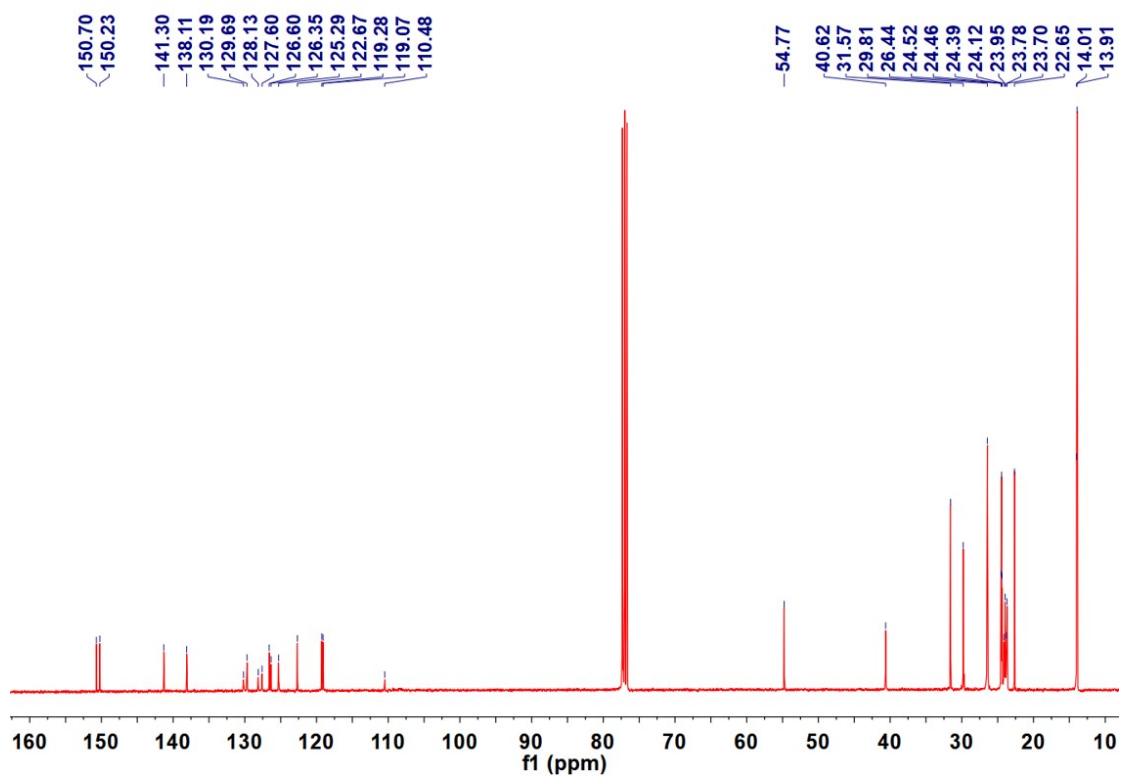


Figure S10. ¹³C NMR spectrum (101 MHz, CDCl₃, 298 K) of Pt-1b.

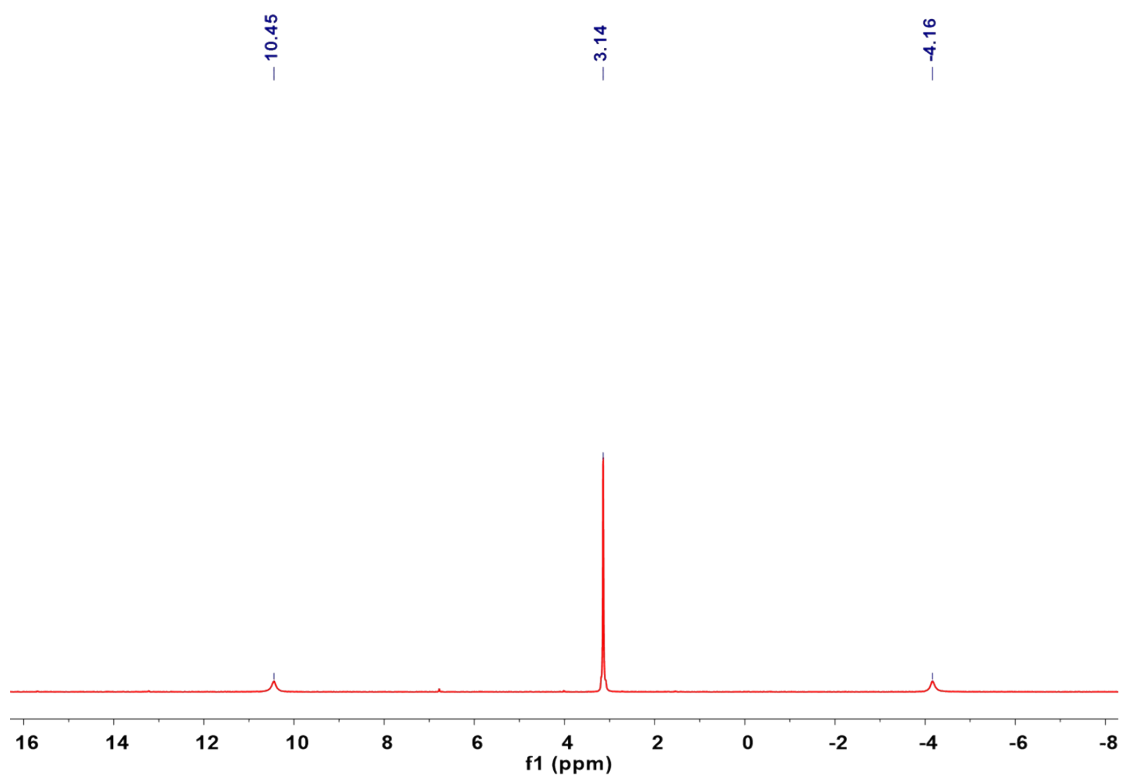


Figure S11. $^{31}\text{P}\{^1\text{H}\}$ NMR spectrum (162 MHz, CDCl_3 , 298 K) of Pt-1b.

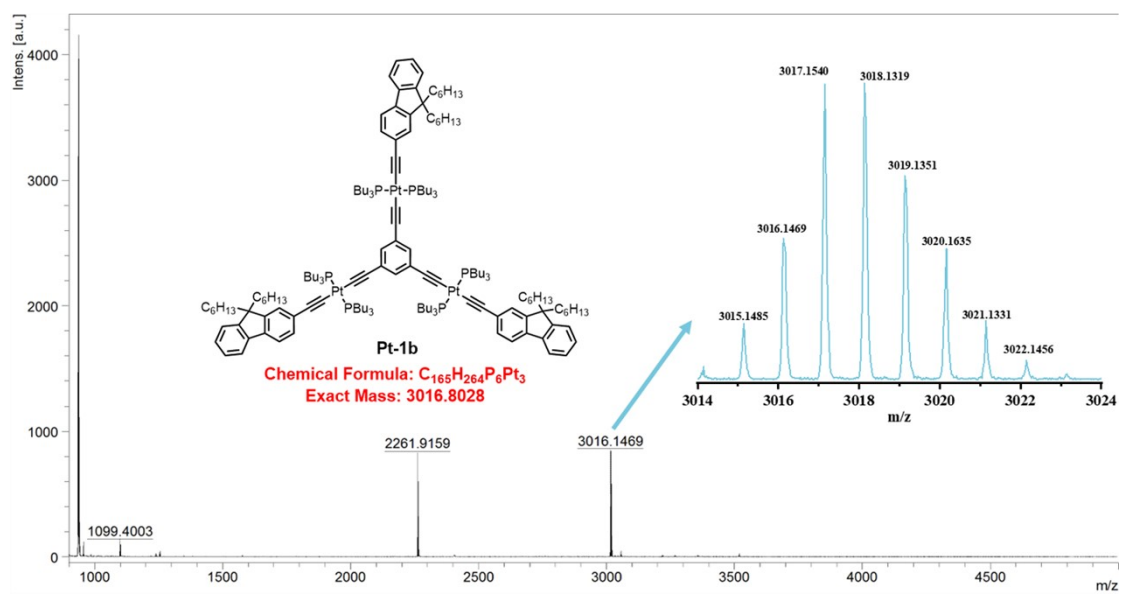


Figure S12. MALDI-TOF-MS spectrum of Pt-1b.

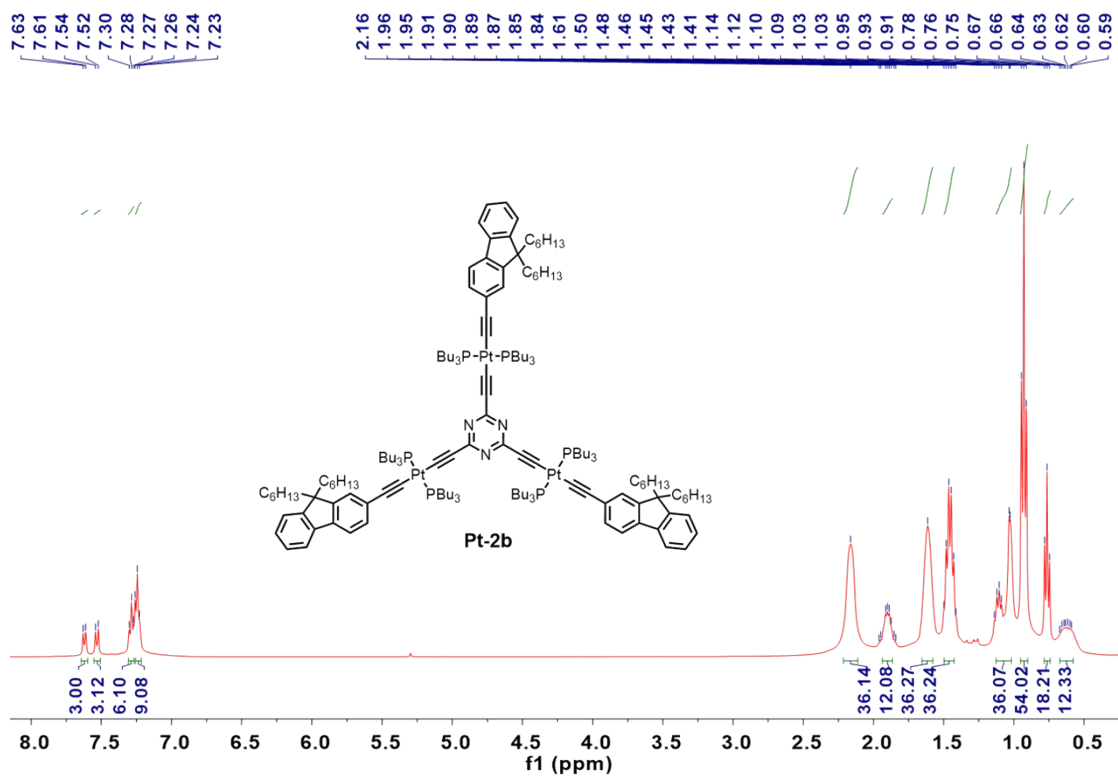


Figure S13. ^1H NMR spectrum (400 MHz, CDCl_3 , 298 K) of Pt-2b.

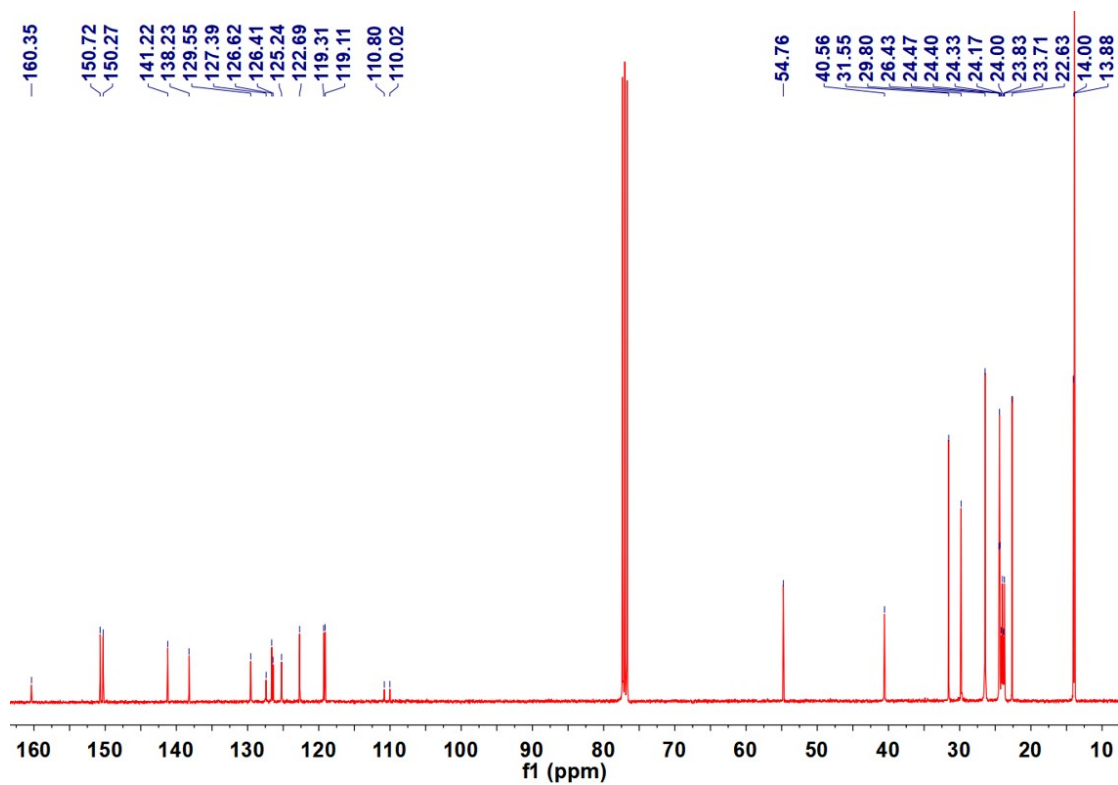


Figure S14. ^{13}C NMR spectrum (101 MHz, CDCl_3 , 298 K) of Pt-2b.

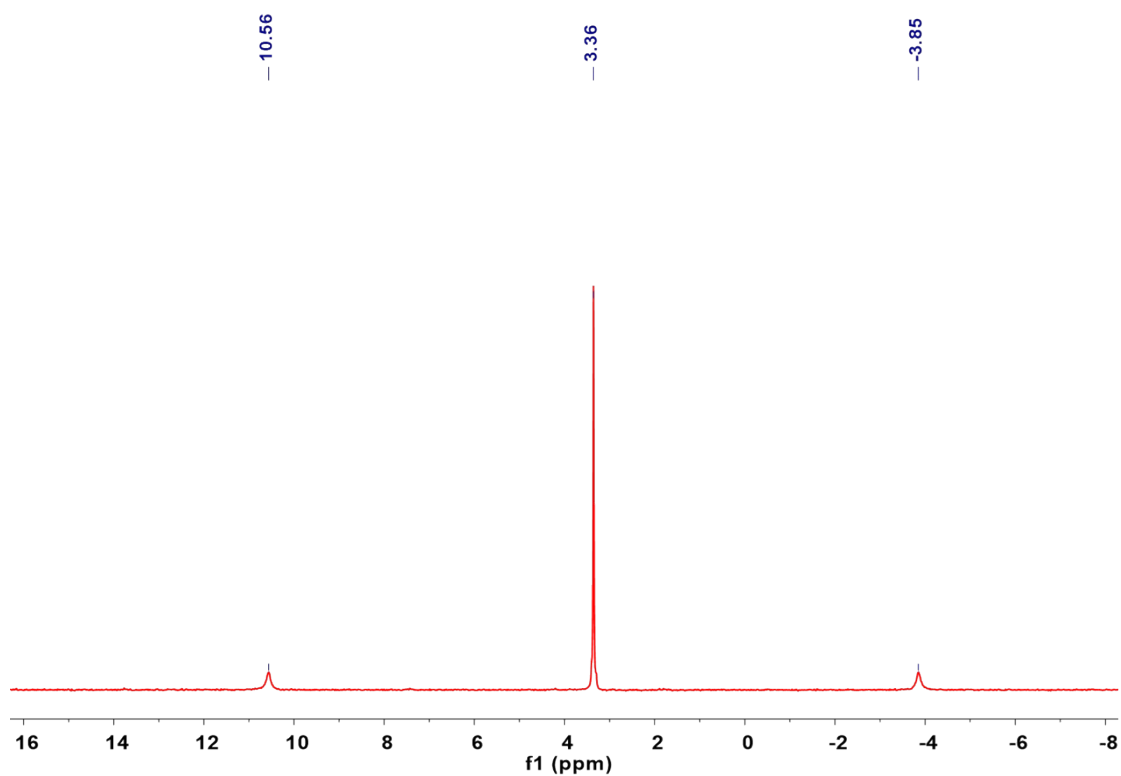


Figure S15. $^{31}\text{P}\{^1\text{H}\}$ NMR spectrum (162 MHz, CDCl_3 , 298 K) of Pt-2b.

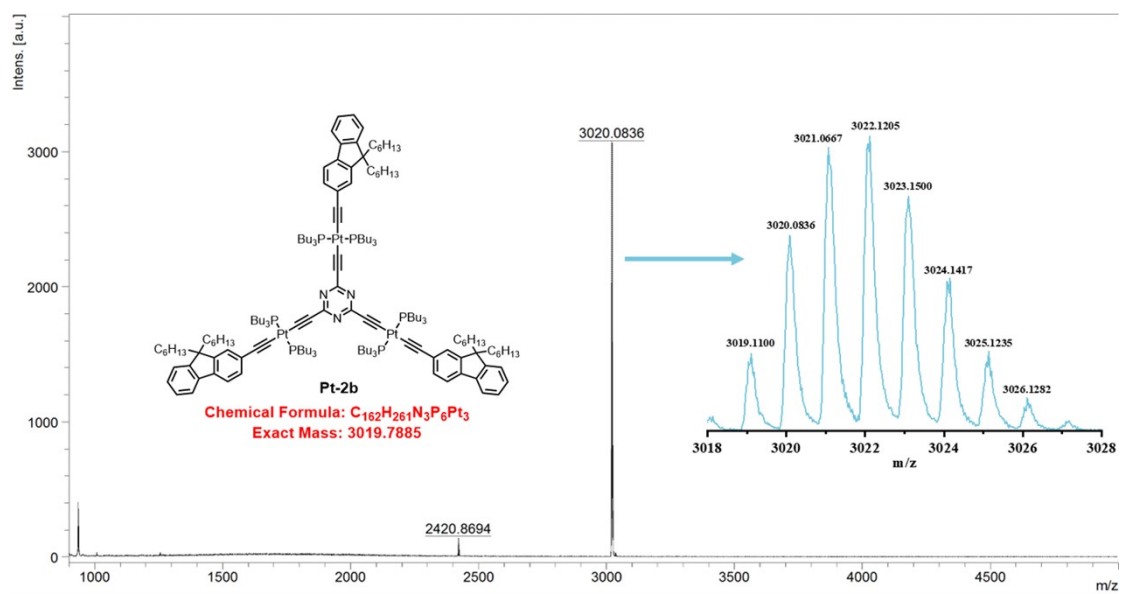


Figure S16. MALDI-TOF-MS spectrum of Pt-2b.

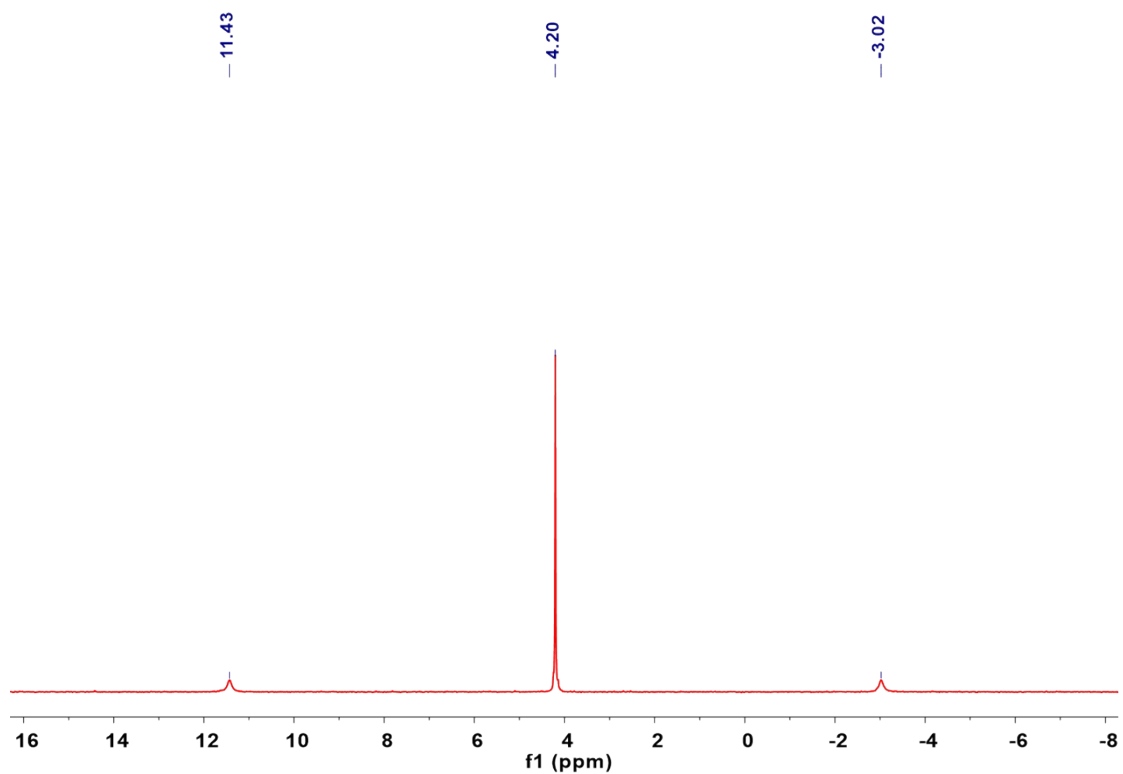


Figure S19. $^{31}\text{P}\{^1\text{H}\}$ NMR spectrum (162 MHz, CDCl_3 , 298 K) of Pt-1c.

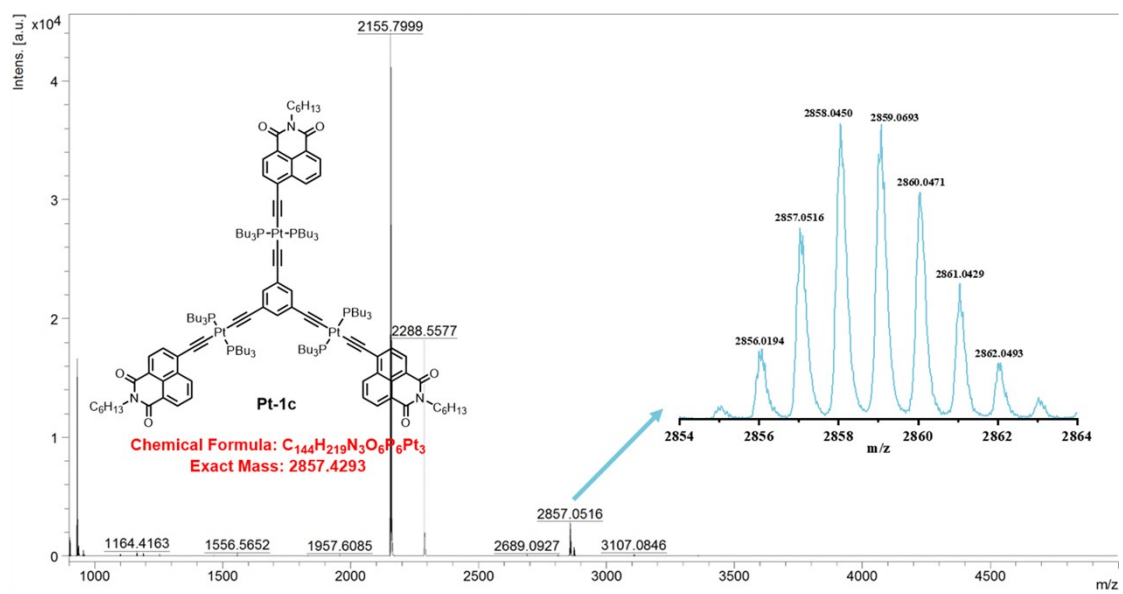


Figure S20. MALDI-TOF-MS spectrum of Pt-1c.

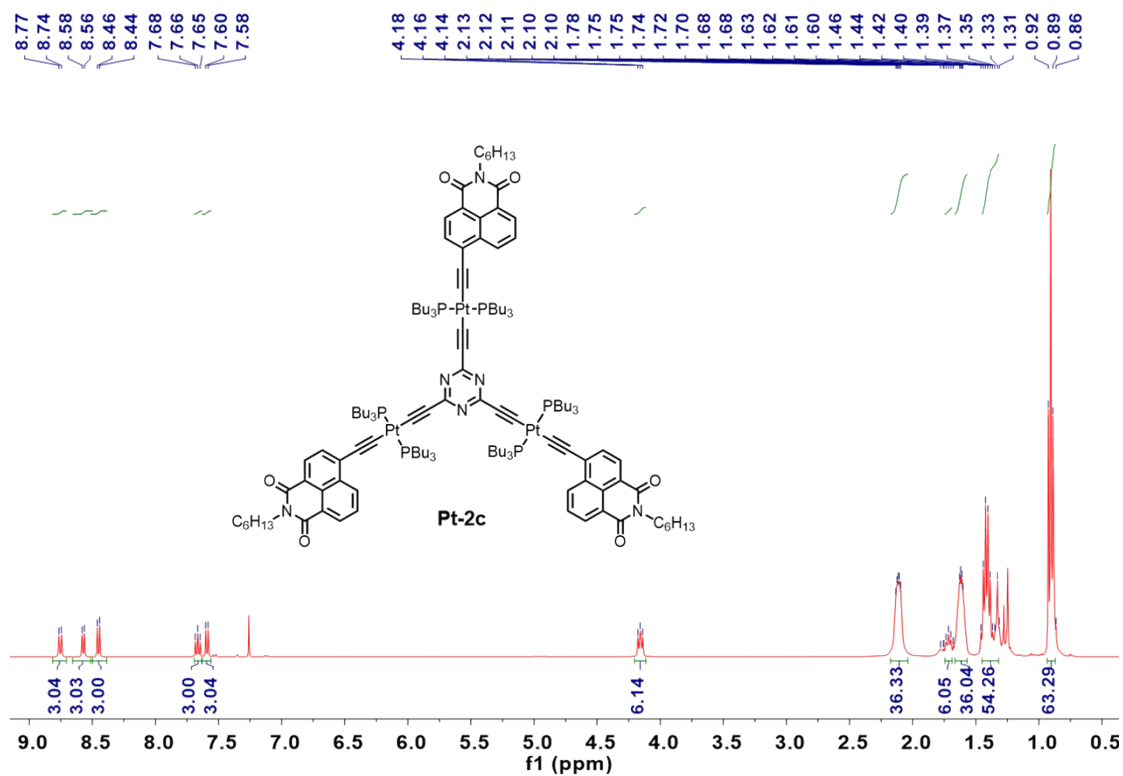


Figure S21. ¹H NMR spectrum (400 MHz, CDCl₃, 298 K) of Pt-2c.

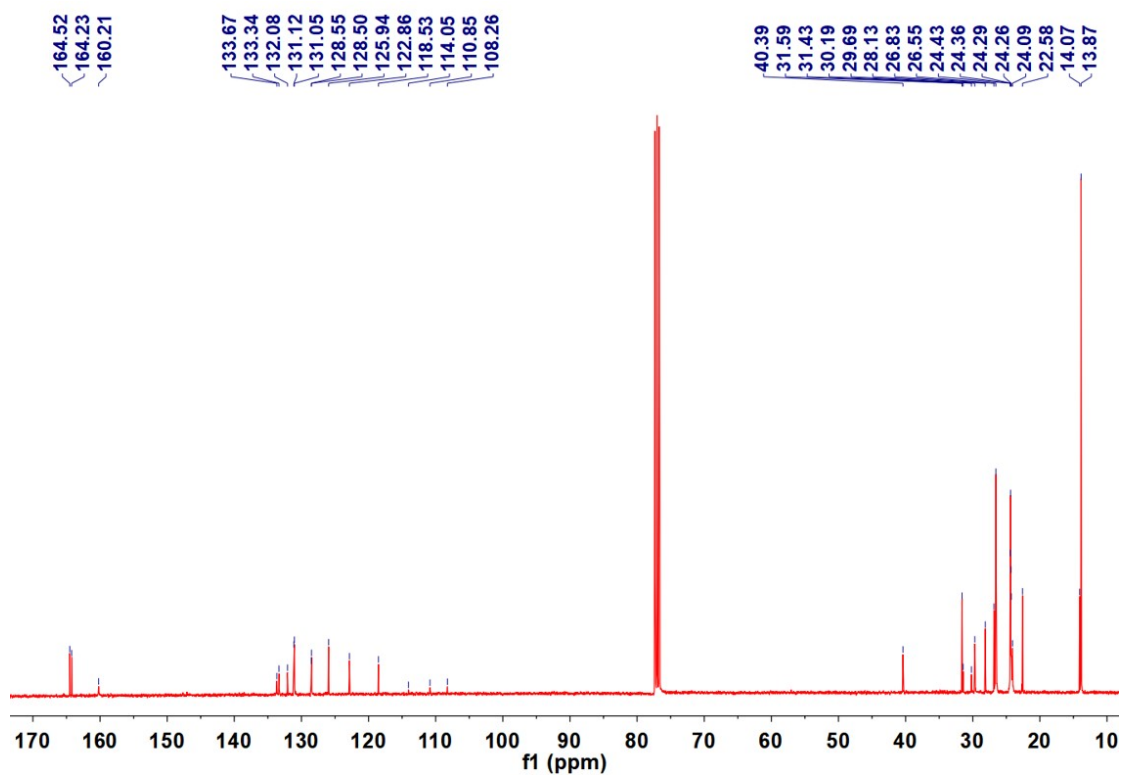


Figure S22. ¹³C NMR spectrum (101 MHz, CDCl₃, 298 K) of Pt-2c.

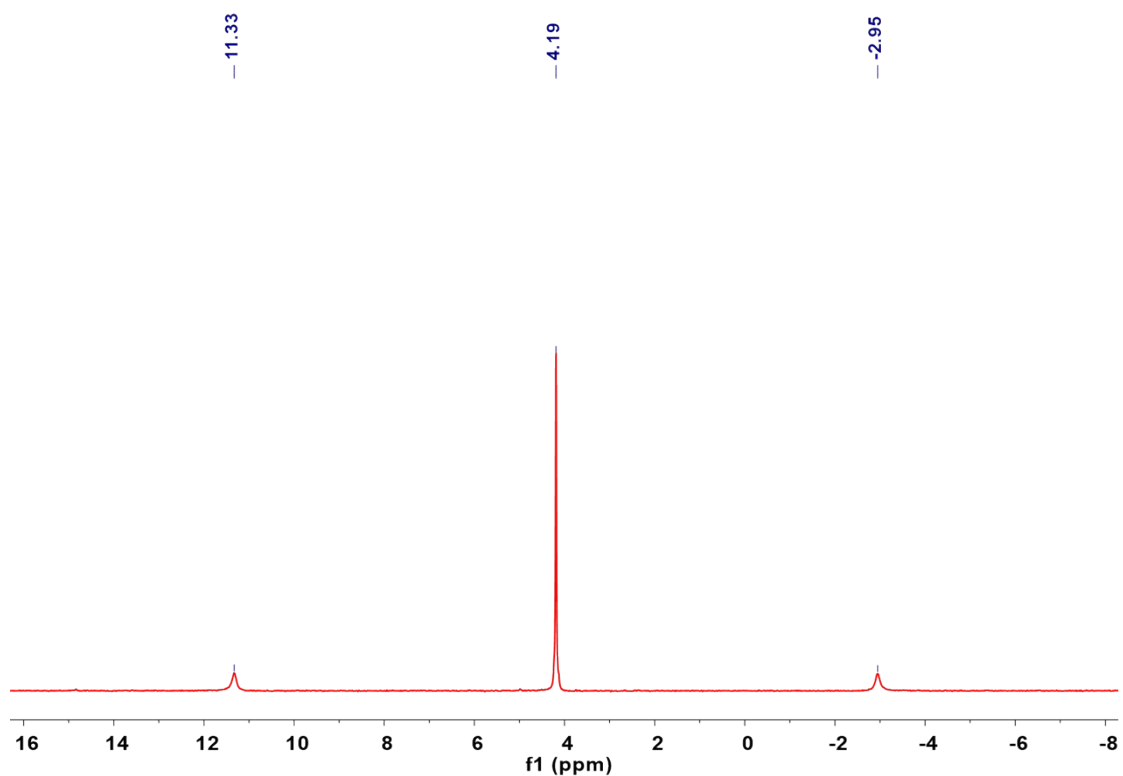


Figure S23. $^{31}\text{P}\{^1\text{H}\}$ NMR spectrum (162 MHz, CDCl_3 , 298 K) of Pt-2c.

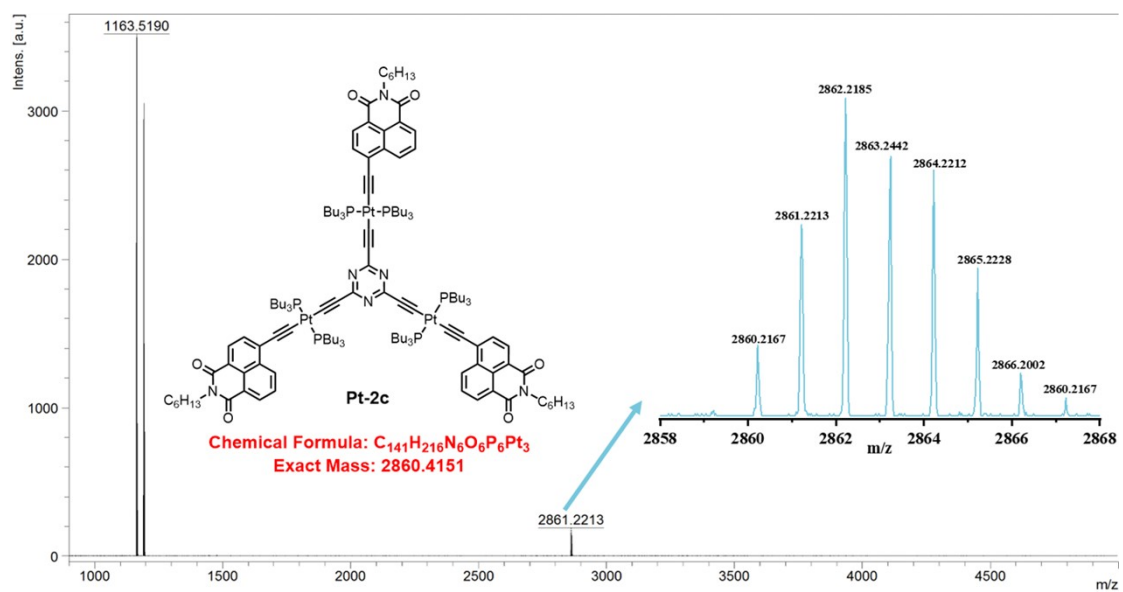


Figure S24. MALDI-TOF-MS spectrum of Pt-2c.

3. Stability Study

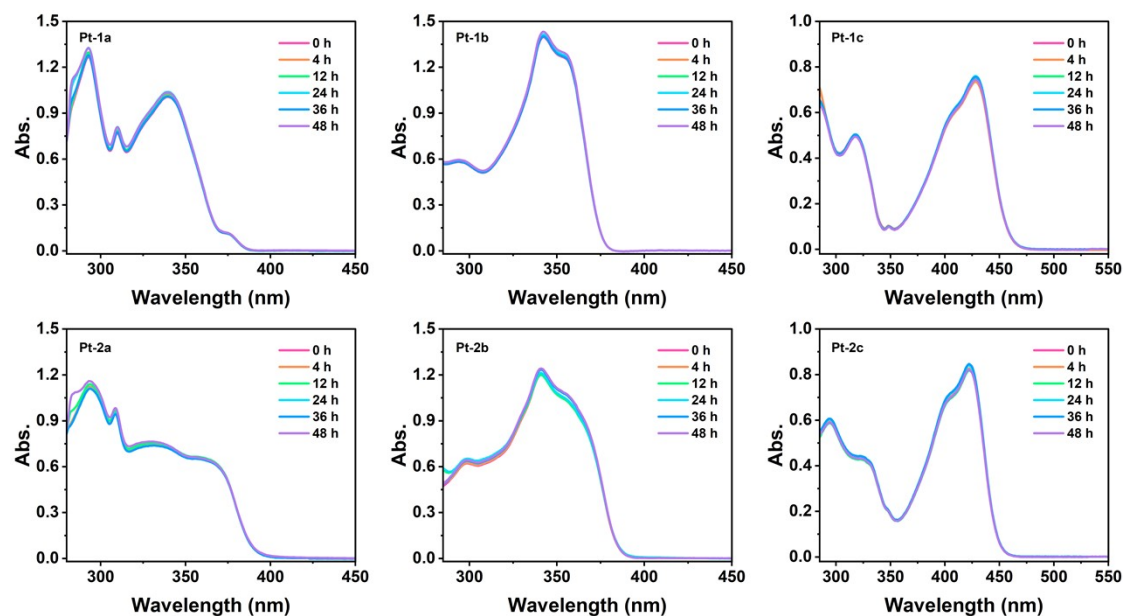


Figure S25. UV-vis absorption spectra of **Pt-1a–Pt-2c** in toluene solution for various time periods ($c = 1.0 \times 10^{-5} \text{ mol L}^{-1}$, r.t.).

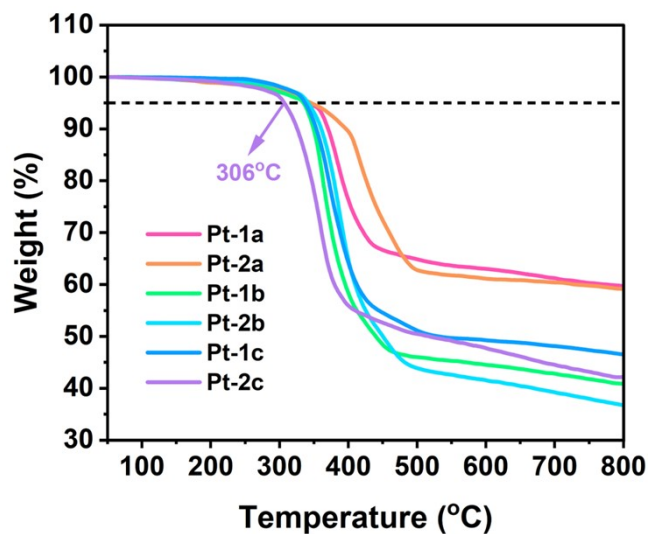


Figure S26. Thermogravimetric analysis curves of **Pt-1a–Pt-2c**.

4. X-ray Crystal Structures

Table S1. Crystal data and structure refinement for **Pt-1b** and **Pt-2b**.

Identification	Pt-1b	Pt-2b
CCDC No.	2288730	2288731
Empirical formula	$\text{C}_{330}\text{H}_{528}\text{P}_{12}\text{Pt}_6$	$\text{C}_{324}\text{H}_{522}\text{N}_6\text{P}_{12}\text{Pt}_6$

Formula weight	6037.67	6043.62
Temperature/K	195.00	193.00
Crystal system	triclinic	triclinic
Space group	<i>P</i> -1	<i>P</i> -1
a/Å	18.5790(4)	23.4510(6)
b/Å	25.2197(5)	23.9387(7)
c/Å	37.9825(8)	34.2530(10)
α /°	94.7760(10)	101.488(2)
β /°	98.0640(10)	106.607(2)
γ /°	109.9000(10)	105.679(2)
Volume/Å ³	16403.9(6)	16926.6(9)
Z	2	2
ρ_{calc} , g/cm ³	1.222	1.186
μ /mm ⁻¹	5.572	5.045
F(000)	6312.0	6312.0
Crystal size/mm ³	0.15 × 0.13 × 0.12	0.15 × 0.12 × 0.11
Radiation	CuK α (λ = 1.54178)	CuK α (λ = 1.54178)
2 θ range for data collection/°	3.764 to 137.266	4.018 to 136.85
Reflections collected	195414	222903
Independent reflections	60085 [R_{int} = 0.0677, R_{sigma} = 0.0543]	61825 [R_{int} = 0.0553, R_{sigma} = 0.0535]
Data/restraints/parameters	60085/9251/3652	61825/9831/3799
Goodness-of-fit on F ²	1.056	1.053
Final R indexes [$I \geq 2\sigma(I)$]	R_1 = 0.0701, wR_2 = 0.1959	R_1 = 0.0918, wR_2 = 0.2838
Final R indexes [all data]	R_1 = 0.0950, wR_2 = 0.2198	R_1 = 0.1089, wR_2 = 0.2982
Largest diff. peak/hole / e Å ⁻³	3.24/-2.98	2.56/-1.95

Table S2. Crystal data and structure refinement for **Pt-1c** and **Pt-2c**.

Identification	Pt-1c	Pt-2c
CCDC No.	2213945	2288732
Empirical formula	C ₁₄₄ H ₂₁₉ N ₃ O ₆ P ₆ Pt ₃	C ₁₄₁ H ₂₁₆ N ₆ O ₆ P ₆ Pt ₃
Formula weight	2859.30	2862.28
Temperature/K	193.00	195.00
Crystal system	triclinic	triclinic
Space group	<i>P</i> -1	<i>P</i> -1
a/Å	18.7424(9)	20.0033(7)
b/Å	20.0929(8)	22.9084(8)
c/Å	22.3154(10)	34.0378(14)
α/°	82.091(2)	99.793(2)
β/°	68.858(2)	103.159(2)
γ/°	68.3640(10)	102.423(2)
Volume/Å ³	7285.7(6)	14433.5(9)
Z	2	4
ρ _{calc} , g/cm ³	1.303	1.317
μ/mm ⁻¹	2.990	6.351
F(000)	2952.0	5904.0
Crystal size/mm ³	0.13 × 0.12 × 0.1	0.13 × 0.12 × 0.1
Radiation	MoKα (λ = 0.71073)	CuKα (λ = 1.54178)
2θ range for data collection/°	3.828 to 50.054	5.34 to 133.188
Reflections collected	106286	124503
Independent reflections	25665 [R _{int} = 0.0651, R _{sigma} = 0.0561]	48978 [R _{int} = 0.1195, R _{sigma} = 0.1521]
Data/restraints/parameters	25665/4083/1599	48978/4154/3039
Goodness-of-fit on F ²	1.044	0.958
Final R indexes [I ≥ 2σ (I)]	R ₁ = 0.0902, wR ₂ =	R ₁ = 0.0922, wR ₂ = 0.2348

	0.2560	
Final R indexes [all data]	$R_1 = 0.1187$	$wR_2 = 0.1681, wR_2 = 0.3073$
	0.2937	
Largest diff. peak/hole / $e \text{ \AA}^{-3}$	3.55/-2.95	1.69/-0.88

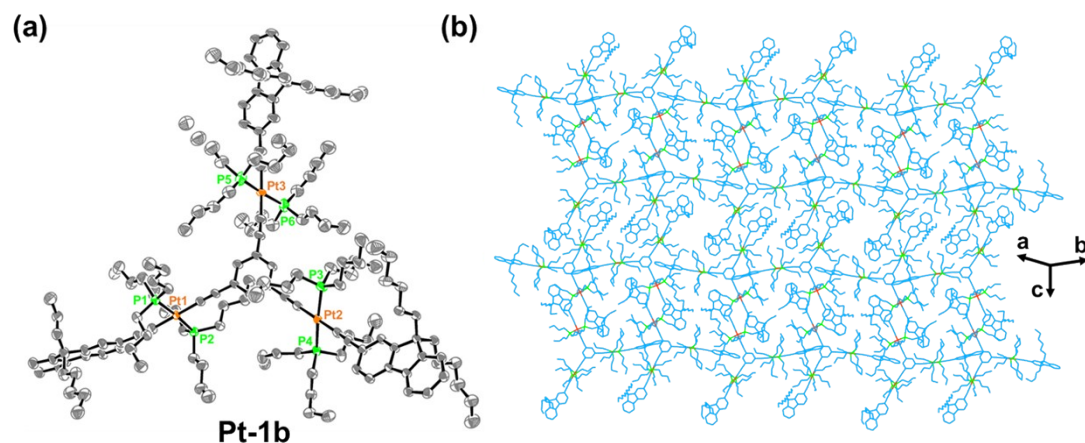


Figure S27. (a) ORTEP diagram of **Pt-1b**. (Ellipsoids are drawn at the 30% probability level). (b) Crystal stacking model of **Pt-1b**. H atoms are omitted for clarity.

Table S3. Selected bond distances and bond angles with estimated standard deviations (Esd's) in parentheses for **Pt-1b**.

Bond Distances (Å)			
Pt1-C1	1.990(10)	Pt2-P3	2.291(3)
Pt1-C52	2.007(9)	Pt2-P4	2.287(2)
Pt1-P1	2.296(2)	Pt3-C113	1.987(10)
Pt1-P2	2.303(2)	Pt3-C326	1.996(12)
Pt2-C60	1.995(9)	Pt3-P5	2.251(4)
Pt2-C85	2.008(8)	Pt3-P6	2.283(4)
Bond Angles (°)			
C1-Pt1-C52	179.2(4)	C1-Pt1-P2	87.1(3)
P1-Pt1-P2	175.4(9)	C52-Pt1-P1	92.1(3)
C1-Pt1-P1	88.5(3)	C52-Pt1-P2	92.4(3)

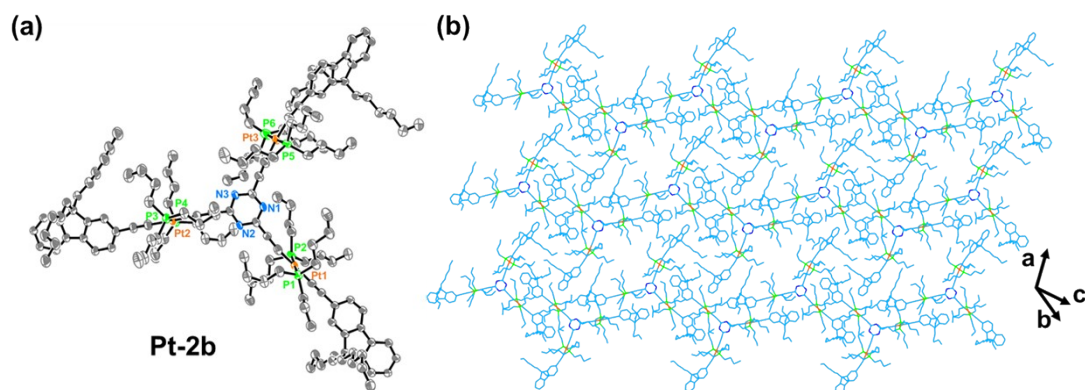


Figure S28. (a) ORTEP diagram of **Pt-2b**. (Ellipsoids are drawn at the 30% probability level). (b) Crystal stacking model of **Pt-2b**. H atoms are omitted for clarity.

Table S4. Selected bond distances and bond angles with estimated standard deviations (Esd's) in parentheses for **Pt-2b**.

Bond Distances (Å)			
Pt1-C187	2.067(13)	Pt2-P3	2.286(4)
Pt1-C214	1.852 (16)	Pt2-P4	2.302(4)
Pt1-P1	2.299(3)	Pt3-C273	1.997(14)
Pt1-P2	2.305(3)	Pt3-C298	1.993(14)
Pt2-C219	1.979(13)	Pt3-P5	2.295(4)
Pt2-C244	1.992(14)	Pt3-P6	2.315(13)
Bond Angles (°)			
C187-Pt1-C214	177.9(6)	C187-Pt1-P2	92.1(4)
P1-Pt1-P2	178.1(11)	C214-Pt1-P1	92.7(4)
C187-Pt1-P1	88.3(4)	C214-Pt1-P2	87.0(4)

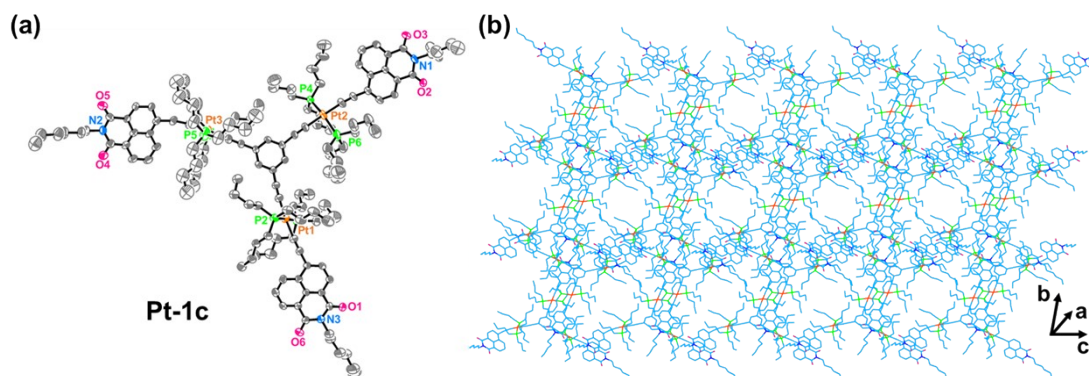


Figure S29. (a) ORTEP diagram of **Pt-1c**. (Ellipsoids are drawn at the 30% probability level). (b) Crystal stacking model of **Pt-1c**. H atoms are omitted for clarity.

Table S5. Selected bond distances and bond angles with estimated standard deviations (Esd's) in parentheses for **Pt-1c**.

Bond Distances (Å)			
Pt1-C9	1.973(11)	Pt2-P4	2.253(5)
Pt1-C38	2.005(11)	Pt2-P6	2.413(7)
Pt1-P1	2.300(3)	Pt3-C26	2.073(11)
Pt1-P2	2.287(3)	Pt3-C64	1.774(12)
Pt2-C27	1.997(11)	Pt3-P3	2.328(4)
Pt2-C47	2.001(12)	Pt3-P5	2.298(4)
Bond Angles (°)			
C9-Pt1-C38	175.4(5)	C9-Pt1-P2	92.6(3)
P1-Pt1-P2	177.9(11)	C38-Pt1-P1	92.7(3)
C9-Pt1-P1	85.4(3)	C38-Pt1-P2	89.2(3)

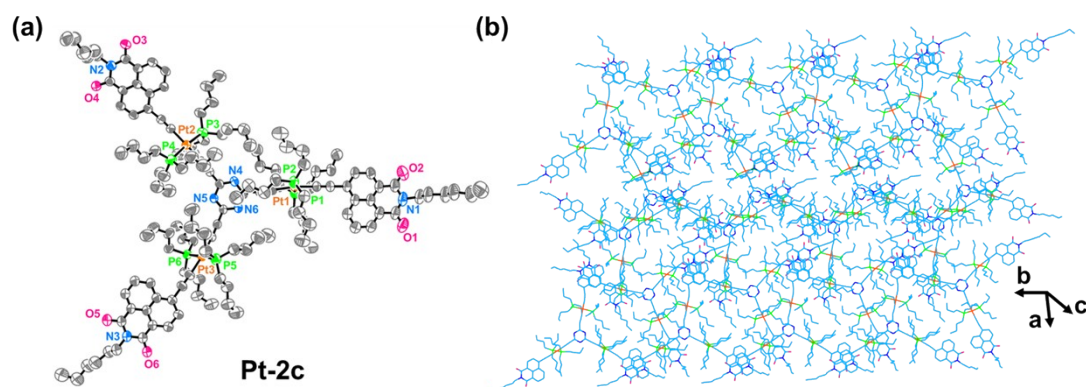


Figure S30. (a) ORTEP diagram of **Pt-2c**. (Ellipsoids are drawn at the 30% probability level). (b) Crystal stacking model of **Pt-2c**. H atoms are omitted for clarity.

Table S6. Selected bond distances and bond angles with estimated standard deviations (Esd's) in parentheses for **Pt-2c**.

Bond Distances (Å)			
Pt1-C21	1.983(17)	Pt2-P3	2.292(6)
Pt1-C11	1.965(17)	Pt2-P4	2.284(6)
Pt1-P1	2.296(5)	Pt3-C33	1.980(17)
Pt1-P2	2.281(5)	Pt3-C15	2.019(17)
Pt2-C36	1.963(17)	Pt3-P5	2.303(5)
Pt2-C13	1.996(17)	Pt3-P6	2.301(14)
Bond Angles (°)			
C11-Pt1-C21	172.2(8)	C11-Pt1-P2	88.4(5)
P1-Pt1-P2	177.4(18)	C21-Pt1-P1	87.8(5)
C11-Pt1-P1	92.2(5)	C21-Pt1-P2	91.3(5)

Table S7. Hydrogen bonds for **Pt-1b**, **Pt-2b**, **Pt-1c**, and **Pt-2c** (Å and °).

Complexes	D-H...A ^[a]	d(D-H)	d(H...A)	d(D...A)	<(DHA)
Pt-1b	C47-H47... π_1	0.98	3.72	4.58	147.74
	C73-H73B... π_2	0.99	2.92	3.87	160.94
	C97-H97... π_3	0.95	2.95	3.75	143.95

Pt-2b	C188–H18S··· π_4	0.99	3.68	4.67	174.21
	C235–H23C··· π_5	0.99	3.25	3.75	112.91
	C50–H50B··· π_6	0.99	3.33	4.26	157.88
	C185–H18E··· π_7	0.99	3.31	4.24	155.61
	C236–H23E··· π_8	0.99	3.30	4.23	157.29
	C256–H256···N2	0.95	2.67	3.47	142.47
Pt-1c	C65–H65A··· π_9	0.98	3.61	4.61	157.93
	C83–H83A··· π_{10}	0.99	2.85	3.84	178.07
	C41–H41A···O5	0.99	2.72	3.53	140.08
Pt-2c	C3–H3B··· π_{11}	0.99	2.67	3.60	155.67
	C7–H7A··· π_{12}	0.99	2.81	3.60	137.27
	C11–H11A··· π_{13}	0.99	2.76	3.79	141.88
	C7–H7A···N6	0.99	2.62	3.59	165.39
	C9–H9A···O1	0.99	2.57	3.43	155.04

[a] π_1 is the centroid of the aromatic ring C247-C252, π_2 is the centroid of the aromatic ring C240-C245, π_3 is the centroid of the aromatic ring C206-C211, π_4 is the centroid of the aromatic ring C94-C99, π_5 is the centroid of the aromatic ring C87-C92, π_6 is the centroid of the aromatic ring C253-C258, π_7 is the centroid of the aromatic ring C138-C143, π_8 is the centroid of the aromatic ring C144-C149, π_9 and π_{10} are the centroid of the naphthalimide unit in **Pt-1c**, π_{11} and π_{13} are the centroid of the naphthalimide unit in **Pt-2c**, π_{12} is the centroid of the triazine core.

5. Photophysical Properties

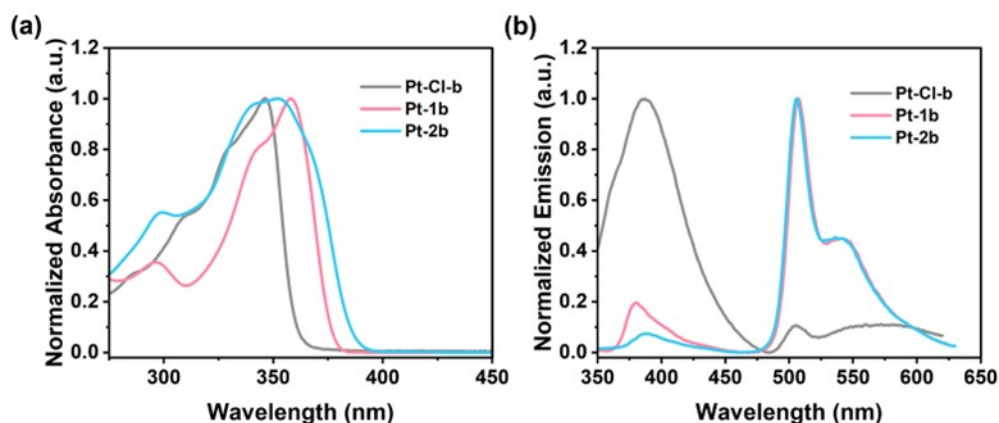


Figure S31. (a) Normalized UV-vis absorption spectra of **Pt-Cl-b**, **Pt-1b**, and **Pt-2b** in CH_2Cl_2 .

(b) Normalized emission spectra of **Pt-Cl-b**, **Pt-1b**, and **Pt-2b** in deaerated CH_2Cl_2 ($c = 1.0 \times 10^{-5}$ mol L^{-1} , r.t.).

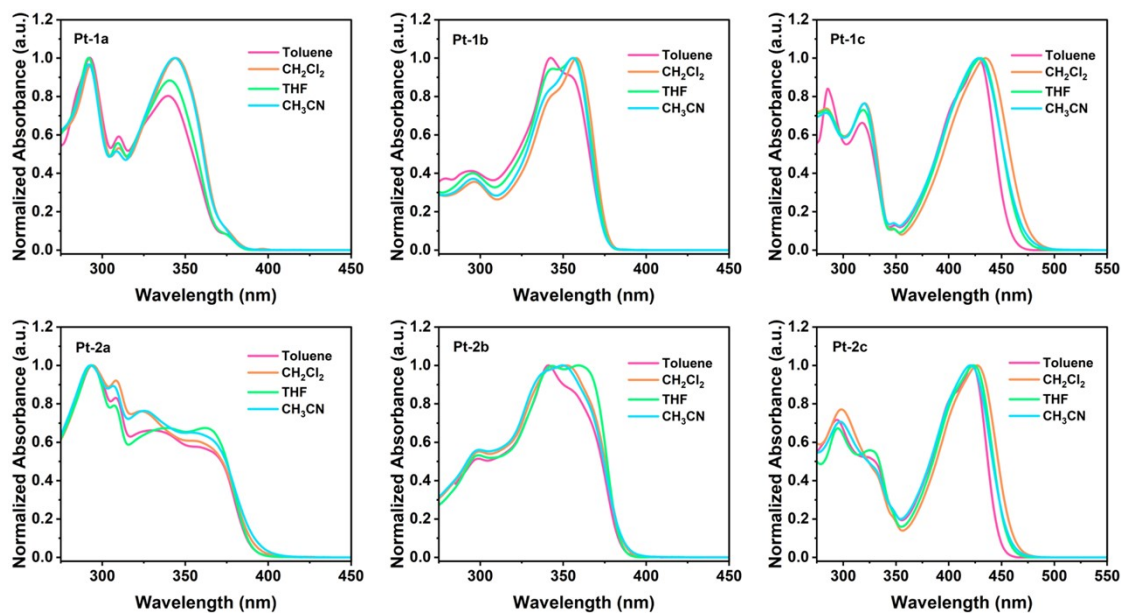


Figure S32. Normalized UV-vis absorption spectra of **Pt-1a–Pt-2c** in different solvents ($c = 1.0 \times 10^{-5}$ mol L^{-1} , r.t.).

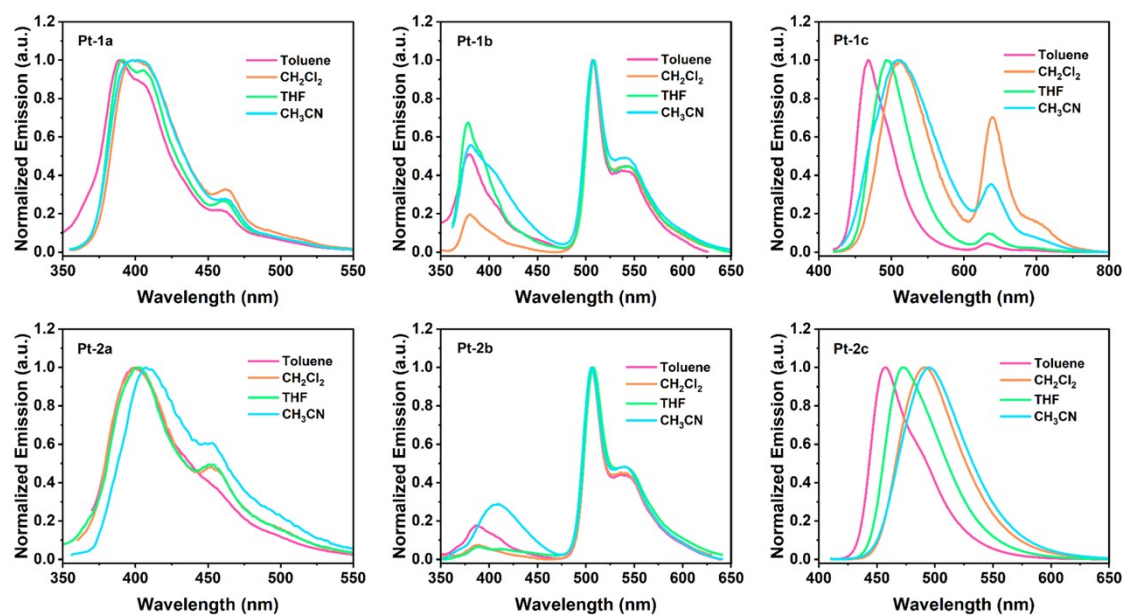


Figure 33. Normalized emission spectra of **Pt-1a–Pt-2c** in different solvents ($c = 1.0 \times 10^{-5}$ mol L^{-1} , r.t.).

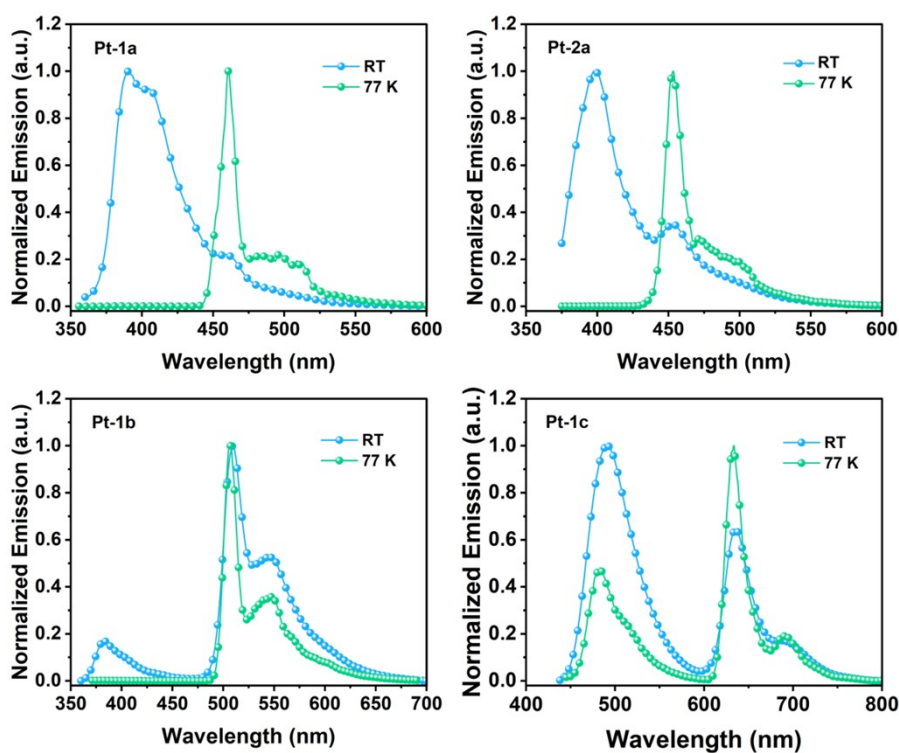


Figure 34. Normalized emission spectra of **Pt-1a**, **Pt-2a**, **Pt-1b**, and **Pt-1c** in 2-Me THF at RT and 77 K ($c = 1.0 \times 10^{-5}$ mol L^{-1}).

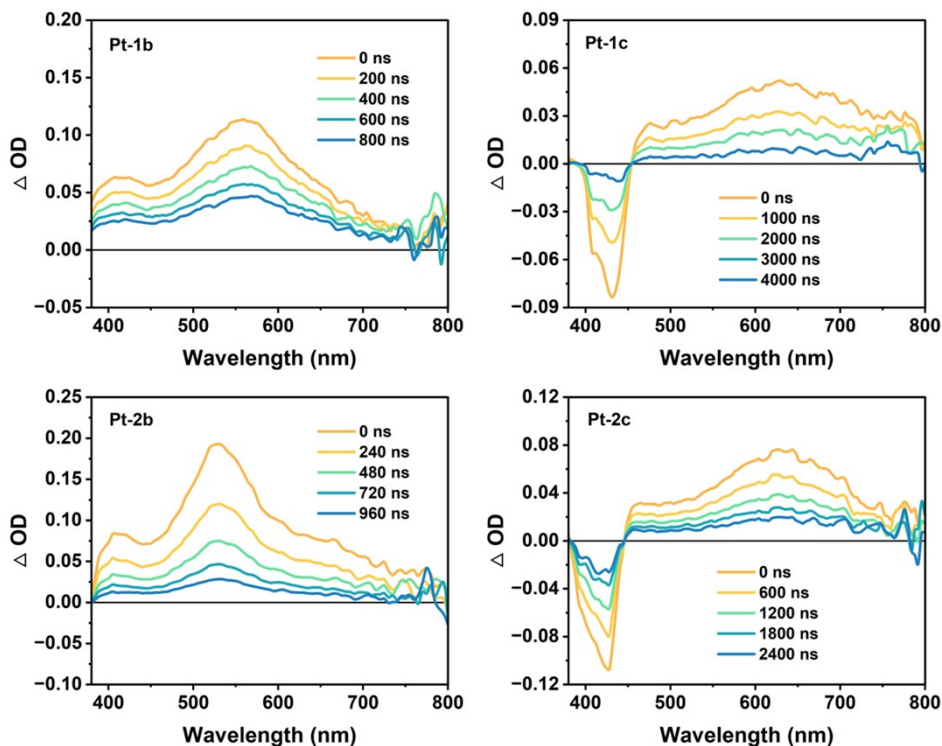


Figure S35. Time-resolved nanosecond transient difference absorption spectra of **Pt-1b**, **Pt-2b**, **Pt-1c**, and **Pt-2c** in deaerated toluene ($\lambda_{\text{ex}} = 355 \text{ nm}$, $c = 1.0 \times 10^{-5} \text{ mol L}^{-1}$).

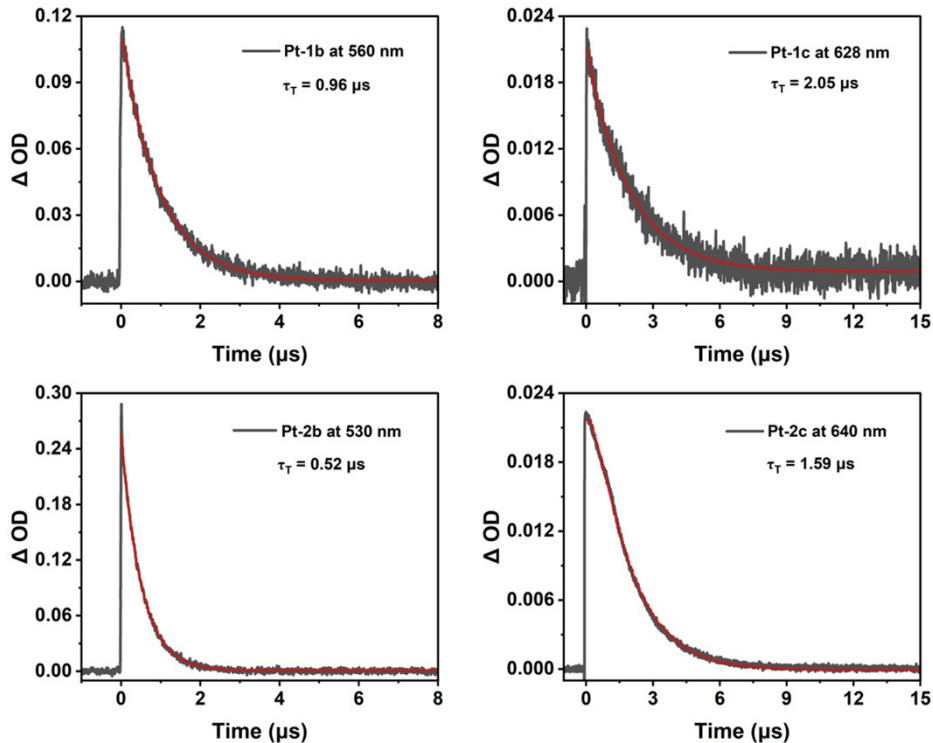


Figure S36. Kinetic curves of **Pt-1b**, **Pt-2b**, **Pt-1c**, and **Pt-2c** in deaerated toluene ($\lambda_{\text{ex}} = 355 \text{ nm}$, $c = 1.0 \times 10^{-5} \text{ mol L}^{-1}$).

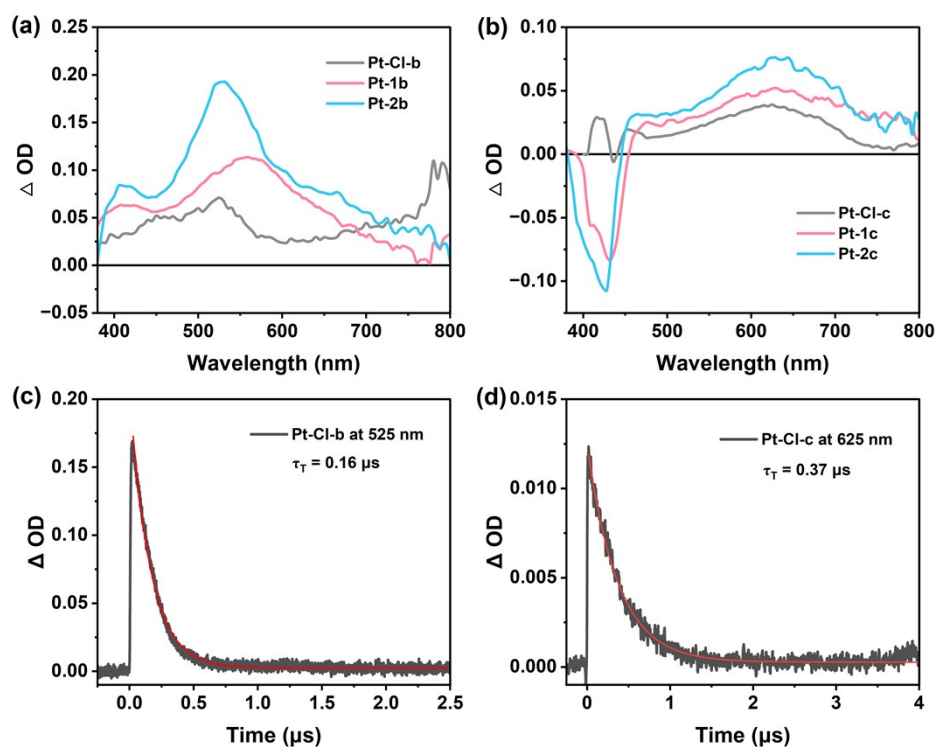


Figure S37. (a) Nanosecond transient absorption spectra of **Pt-Cl-b**, **Pt-1b** and **Pt-2b**. (b)

Nanosecond transient absorption spectra of **Pt-Cl-c**, **Pt-**

1c and **Pt-2c**. (c-d) Kinetic curve of **Pt-Cl-b** and **Pt-Cl-c** in deaerated toluene. ($\lambda_{\text{ex}} = 355 \text{ nm}$, $c = 1.0 \times 10^{-5} \text{ mol L}^{-1}$).

6. Theoretical Calculations

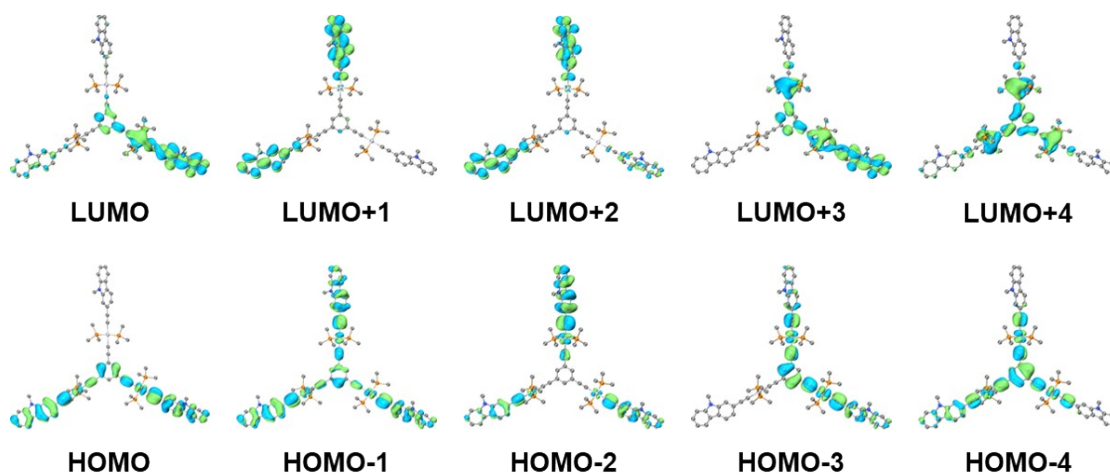


Figure S38. The five highest occupied molecular orbitals (HOMOs) and five lowest unoccupied molecular orbitals (LUMOs) involved in the S_1 and T_1 transitions of **Pt-1a**.

Table S8. Molecular orbitals (MOs) results for **Pt-1a** based on the optimized S_0 geometries.

Orbitals	Energy (eV)	Contribution percentages of fragments to MO (%)			
		Pt atoms	PMe ₃	Core	Ethynyl ligands
LUMO+4	-0.46	19.30	41.70	25.90	11.40
LUMO+3	-0.54	12.90	26.50	20.80	38.30
LUMO+2	-0.58	2.78	5.50	2.19	89.40
LUMO+1	-0.58	1.63	3.46	2.11	92.80
LUMO	-0.60	7.95	15.60	15.50	59.60
HOMO	-4.75	14.40	4.19	16.30	65.00
HOMO-1	-4.76	13.60	4.40	14.10	67.80
HOMO-2	-4.79	10.40	5.49	3.18	80.90
HOMO-3	-4.91	21.40	4.16	43.30	30.90
HOMO-4	-4.98	20.90	5.26	47.80	25.90

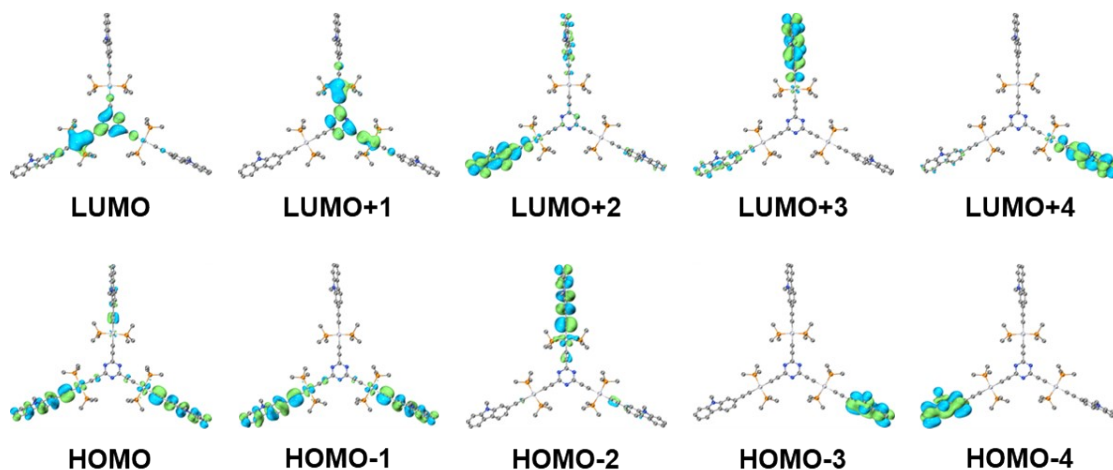


Figure S39. The five highest occupied molecular orbitals (HOMOs) and five lowest unoccupied molecular orbitals (LUMOs) involved in the S_1 and T_1 transitions of **Pt-2a**.

Table S9. Molecular orbitals (MOs) results for **Pt-2a** based on the optimized S_0 geometries.

Orbitals	Energy (eV)	Contribution percentages of fragments to MO (%)			
		Pt atoms	PMe ₃	Core	Ethynyl ligands
LUMO+4	-0.61	1.79	3.36	0.53	94.60
LUMO+3	-0.62	1.70	3.72	0.73	94.30
LUMO+2	-0.63	4.85	15.10	3.57	81.30
LUMO+1	-1.14	11.40	17.66	66.20	4.79
LUMO	-1.15	11.10	17.20	65.00	6.85
HOMO	-4.83	10.10	12.40	2.26	82.10
HOMO-1	-4.84	9.99	14.30	2.03	82.40
HOMO-2	-4.85	9.39	6.12	1.59	83.20
HOMO-3	-5.15	0.01	0.03	0.01	99.90
HOMO-4	-5.16	0.01	0.04	0.01	99.90

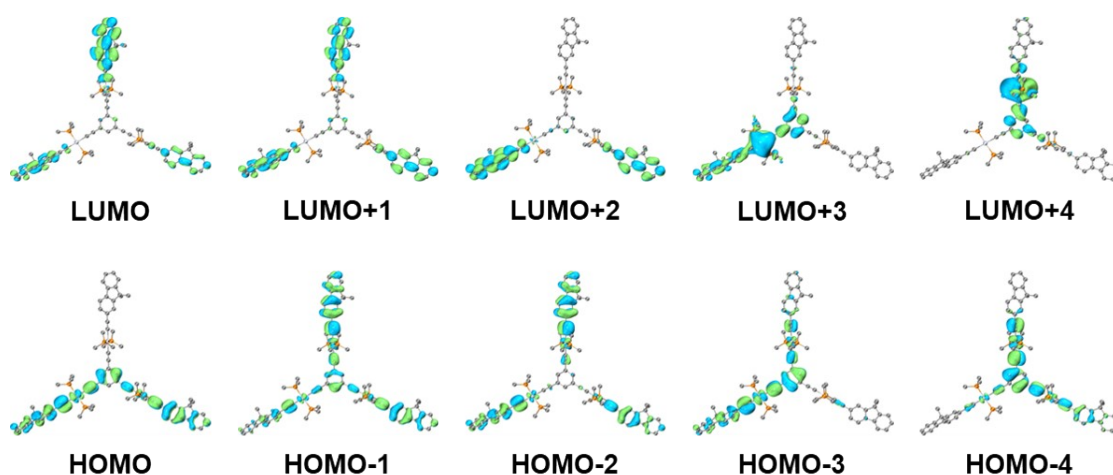


Figure S40. The five highest occupied molecular orbitals (HOMOs) and five lowest unoccupied molecular orbitals (LUMOs) involved in the S₁ and T₁ transitions of **Pt-1b**.

Table S10. Molecular orbitals (MOs) results for **Pt-1b** based on the optimized S₀ geometries.

Orbitals	Energy (eV)	Contribution percentages of fragments to MO (%)
----------	-------------	---

		Pt atoms	PMe ₃	Core	Ethynyl ligands
LUMO+4	-0.39	42.00	48.10	22.00	9.93
LUMO+3	-0.56	45.90	35.10	30.10	19.00
LUMO+2	-0.70	5.52	6.19	2.39	88.30
LUMO+1	-0.70	6.26	6.44	3.13	87.30
LUMO	-0.71	3.07	6.25	2.41	88.30
HOMO	-4.78	3.12	3.92	21.30	58.30
HOMO-1	-4.80	3.13	4.50	14.30	67.40
HOMO-2	-4.83	15.80	5.39	3.29	80.10
HOMO-3	-4.93	20.00	4.41	38.90	36.40
HOMO-4	-5.05	24.10	6.19	52.10	21.40

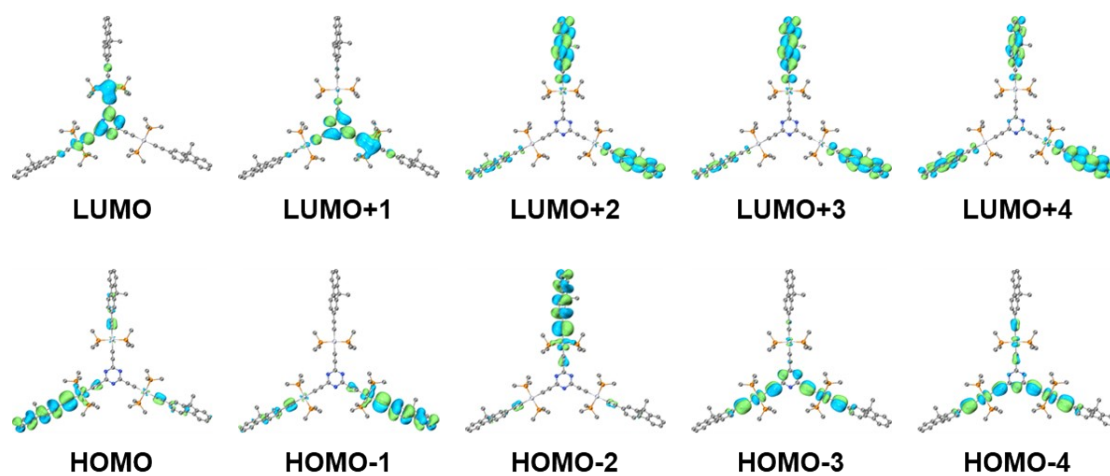


Figure S41. The five highest occupied molecular orbitals (HOMOs) and five lowest unoccupied molecular orbitals (LUMOs) involved in the S₁ and T₁ transitions of **Pt-2b**.

Table S11. Molecular orbitals (MOs) results for **Pt-2b** based on the optimized S₀ geometries.

Orbitals	Energy (eV)	Contribution percentages of fragments to MO (%)			
		Pt atoms	PMe ₃	Core	Ethynyl

					ligands
LUMO+4	-0.72	2.03	2.93	1.87	92.90
LUMO+3	-0.72	1.78	2.99	0.93	94.00
LUMO+2	-0.74	2.58	5.48	1.09	90.40
LUMO+1	-1.17	10.80	16.10	66.00	5.08
LUMO	-1.17	11.20	17.40	65.50	2.95
HOMO	-4.89	9.66	5.82	1.82	70.80
HOMO-1	-4.89	9.57	5.63	1.81	81.60
HOMO-2	-4.90	9.67	5.79	1.83	70.40
HOMO-3	-5.36	38.20	1.04	28.40	22.50
HOMO-4	-5.37	39.30	1.07	25.80	24.70

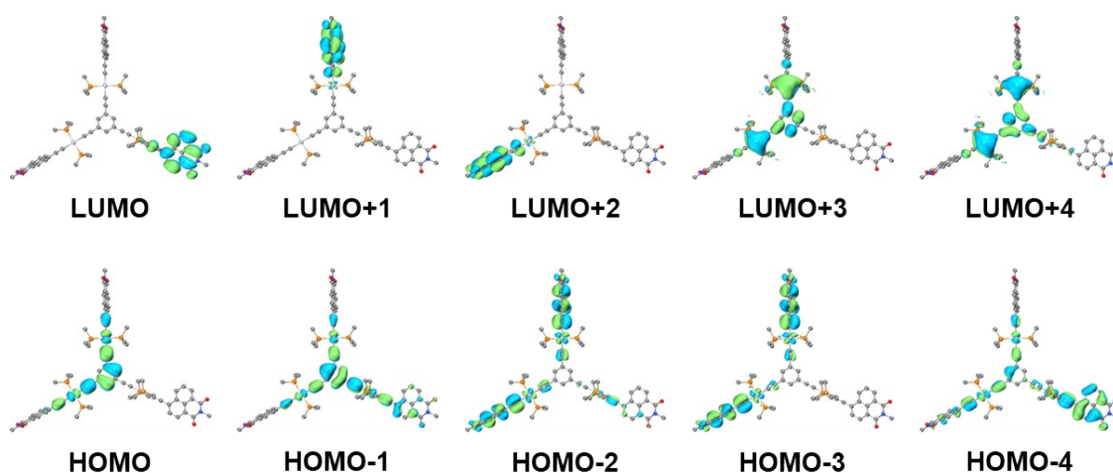


Figure S42. The five highest occupied molecular orbitals (HOMOs) and five lowest unoccupied molecular orbitals (LUMOs) involved in the S_1 and T_1 transitions of **Pt-1c**.

Table S12. Molecular orbitals (MOs) results for **Pt-1c** based on the optimized S_0 geometries.

Orbitals	Energy (eV)	Contribution percentages of fragments to MO (%)			
		Pt atoms	PMe ₃	Core	Ethynyl ligands

LUMO+4	-0.97	19.20	43.10	30.00	7.70
LUMO+3	-1.09	18.20	38.00	36.40	7.46
LUMO+2	-2.16	1.89	2.52	0.26	95.30
LUMO+1	-2.16	1.86	2.50	0.24	95.40
LUMO	-2.17	1.83	2.52	0.23	95.40
HOMO	-5.32	25.80	1.61	59.50	13.10
HOMO-1	-5.38	20.80	3.53	54.10	21.60
HOMO-2	-5.52	12.30	5.49	5.22	76.90
HOMO-3	-5.54	11.00	5.95	3.11	79.90
HOMO-4	-5.57	15.10	5.86	13.10	65.90

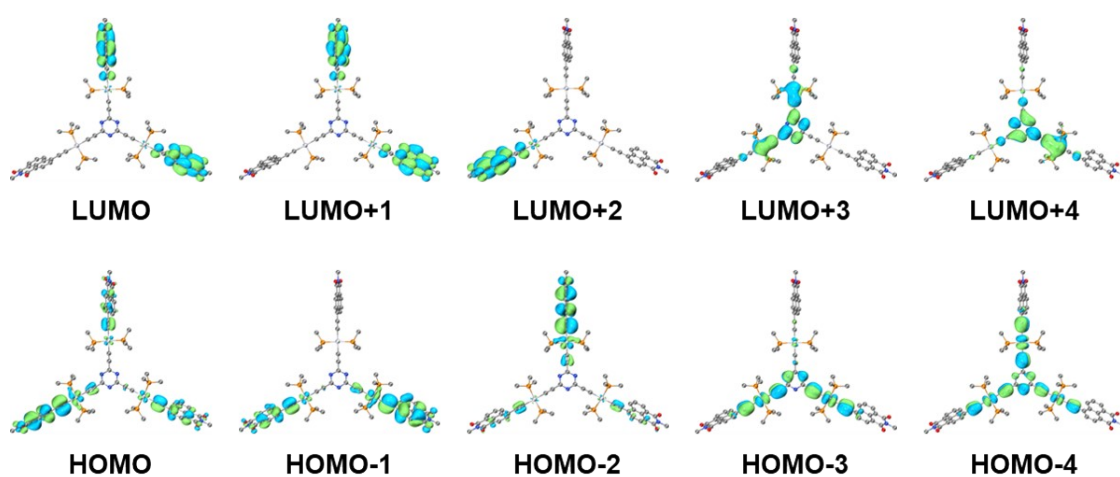


Figure S43. The five highest occupied molecular orbitals (HOMOs) and five lowest unoccupied molecular orbitals (LUMOs) involved in the S_1 and T_1 transitions of **Pt-2c**.

Table S13. Molecular orbitals (MOs) results for **Pt-2c** based on the optimized S_0 geometries.

Orbitals	Energy (eV)	Contribution percentages of fragments to MO (%)			
		Pt atoms	PMe ₃	Core	Ethynyl ligands
LUMO+4	-1.59	11.10	16.40	67.20	5.30

LUMO+3	-1.60	11.60	17.00	66.30	5.08
LUMO+2	-2.20	1.84	2.52	0.22	90.50
LUMO+1	-2.20	1.77	2.54	0.29	95.30
LUMO	-2.20	1.89	2.61	0.40	95.10
HOMO	-5.58	11.00	5.81	2.80	70.60
HOMO-1	-5.58	10.50	6.00	2.32	77.70
HOMO-2	-5.59	10.40	6.00	2.17	80.70
HOMO-3	-5.88	38.10	1.05	32.00	25.70
HOMO-4	-5.89	37.70	1.01	32.60	26.70

Table S14. Natural transition orbitals (NTOs) results for **Pt-1a–Pt-2c** based on their optimized T_1 geometries.

Complexes	NTOs ^[a]	Contribution percentages of fragments to NTOs (%)			
		Pt atoms	PMe ₃	Core	Ethynyl ligands
Pt-1a	P	5.74	5.67	2.99	85.23
	H	11.14	0.93	3.93	83.95
Pt-2a	P	5.70	6.27	5.86	82.17
	H	10.30	1.02	3.19	85.49
Pt-1b	P	4.72	3.86	1.57	89.80
	H	9.04	0.92	2.38	87.70
Pt-2b	P	4.64	4.21	3.78	87.12
	H	8.69	0.92	2.50	87.85
Pt-1c	P	2.56	2.39	0.46	94.58
	H	5.23	2.73	0.99	91.05
Pt-2c	P	4.25	3.13	0.56	92.06
	H	2.29	2.59	0.41	94.72

[a] H and P represent NTO hole and particle orbitals, respectively.

7. Nonlinear Optical Properties

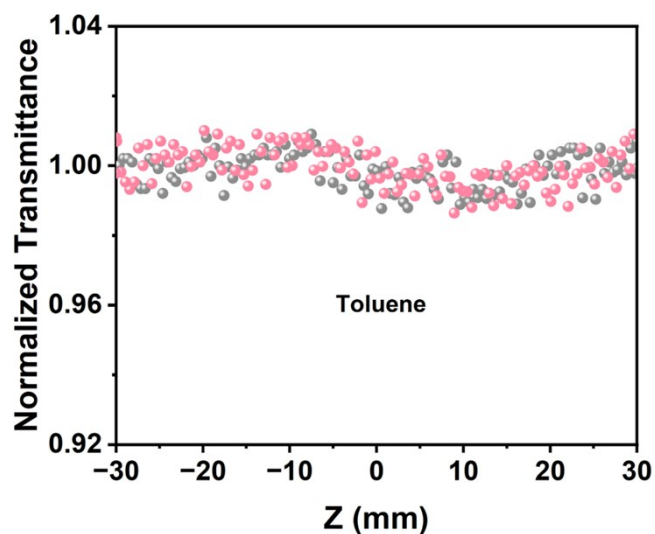


Figure S44. Open-aperture Z-scan curves for toluene at 532 nm.

8. Solid-state Optical Limiter Devices

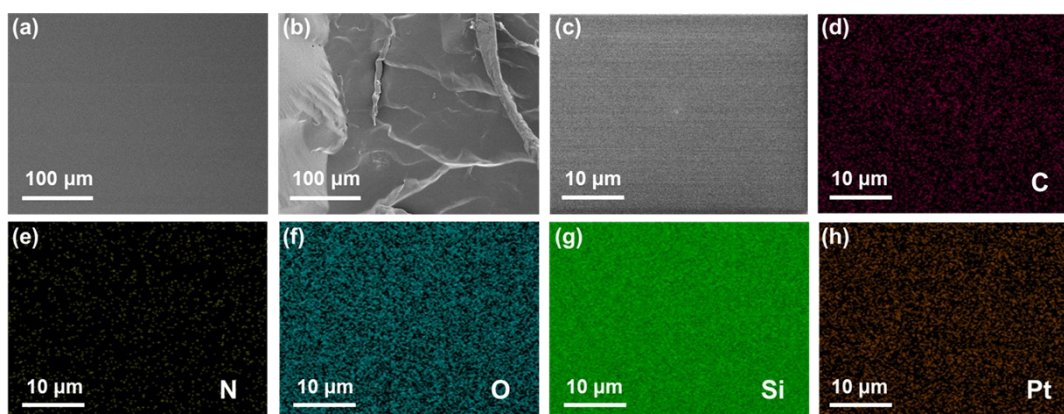


Figure S45. (a) Surface and (b) cross-sectional FE-SEM images of the Pt-2b@PDMS-1.00 wt%, respectively. (c-h) Corresponding elemental mappings of C, N, O, Si and Pt, respectively.

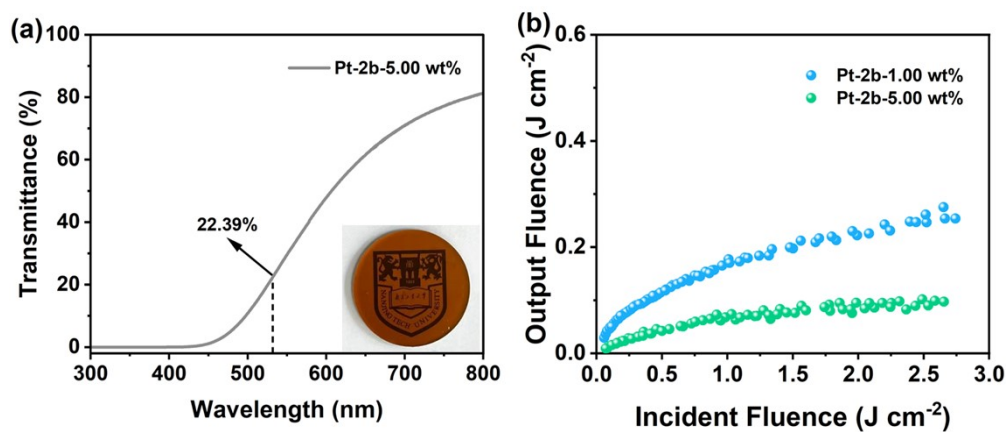


Figure S46. (a) Linear transmittance spectrum of **Pt-2b@PDMS-5.00 wt%** (inset: Optical photograph of **Pt-2b@PDMS-5.00 wt%**). (b) Comparison of the OPL performance between **Pt-2b@PDMS-1.00 wt%** and **Pt-2b@PDMS-5.00 wt%**.

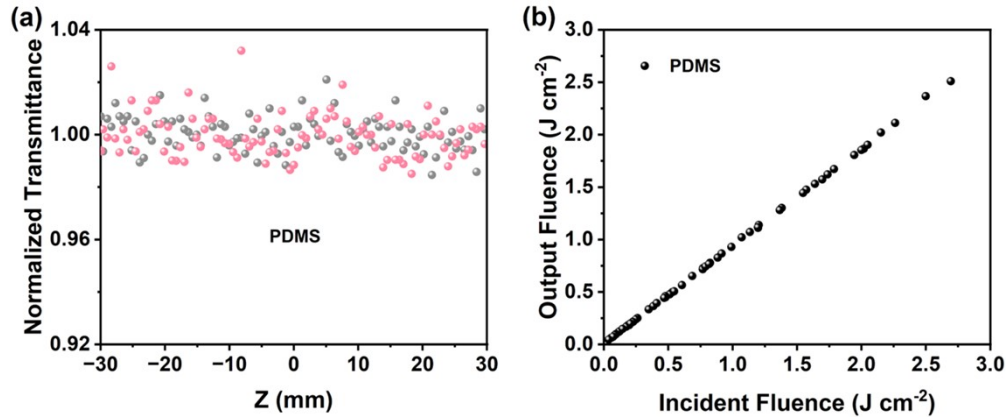


Figure S47. (a) Open-aperture Z-scan curves and (b) output fluence versus input fluence curve for blank PDMS at 532 nm.

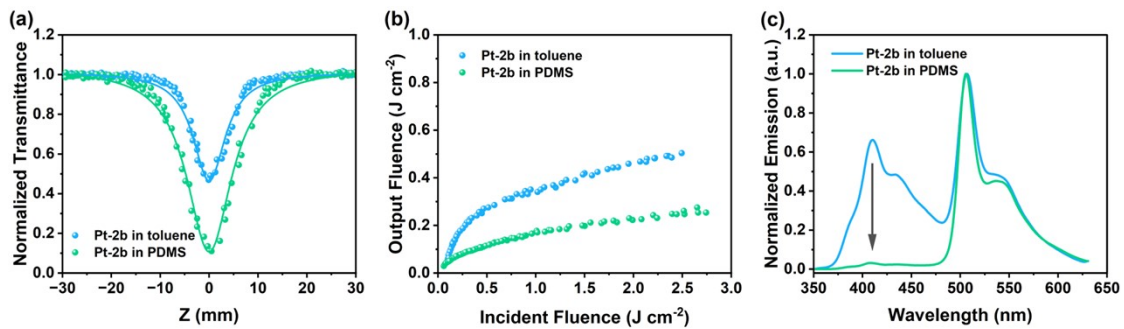


Figure S48. (a) Open-aperture Z-scan curves and (b) output fluence versus input fluence curves for **Pt-2b** in toluene and PDMS matrix at 532 nm. (c) Normalized emission spectra of **Pt-2b** in toluene and PDMS matrix.

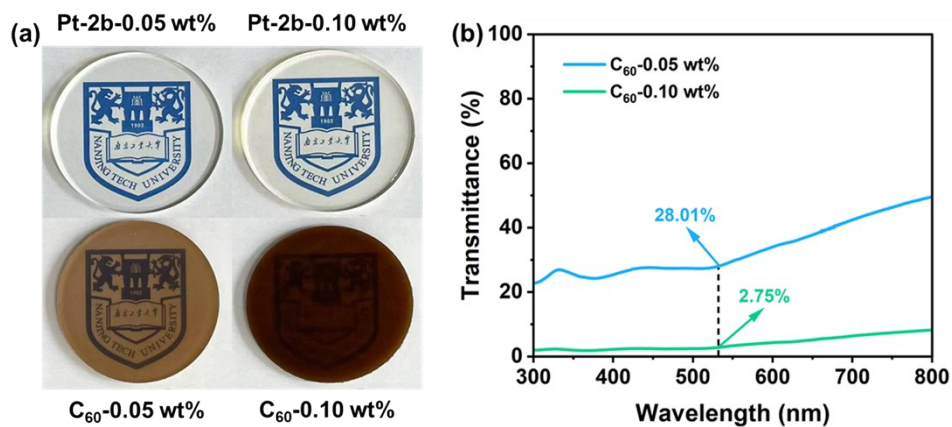


Figure S49. (a) Optical photographs of **Pt-2b@PDMS** and **C₆₀@PDMS** films with various concentrations. (b) Linear transmittance spectra of **C₆₀@PDMS-0.05 wt%** and **C₆₀@PDMS-0.10 wt%**.

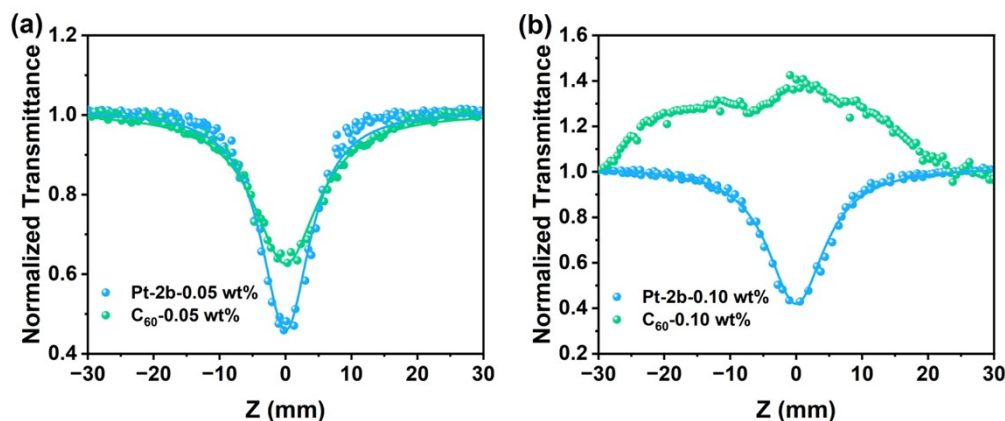


Figure S50. Comparison of the NLO performance between **Pt-2b@PDMS** and **C₆₀@PDMS** films with various concentrations.

Table S15. Linear and nonlinear optical parameters for **Pt-2b@PDMS** films with various concentrations.

Samples	T_0 (%) ^[a]	T_{\min} ^[b]	β_{eff} (cm GW ⁻¹) ^[c]	F_{OL} (J cm ⁻²) ^[d]
blank PDMS	93.19	1	-	-
Pt-2b@PDMS-0.05 wt%	91.35	0.46	317.22	0.57
Pt-2b@PDMS-0.10 wt%	90.45	0.42	394.58	0.52
Pt-2b@PDMS-0.20 wt%	85.56	0.33	513.75	0.39
Pt-2b@PDMS-0.50 wt%	77.28	0.25	650.06	0.33
Pt-2b@PDMS-1.00 wt%	67.09	0.11	965.83	0.26

[a] Linear transmittance at 532 nm (the thickness of all films is 2 mm). [b] The normalized minimum transmittance at the position $Z = 0$. [c] Third-order nonlinear absorption coefficient. [d] Optical limiting threshold.

References

[S1] Grisorio, C. Piliago, P. Fini, P. Cosma, P. Mastroilli, G. Gigli, G. P. Suranna and C. F. Nobile, Influencing the Spectral Stability and the Electroluminescence

- Behavior of New Blue-Emitting Bifluorene-Based Materials by the 7,7'-Functionalization of the Core. *J. Phys. Chem. C*, 2008, **112**, 7005–7014.
- [S2] W. Yang, A. Karatay, J. Zhao, J. Song, L. Zhao, Y. Xing, C. Zhang, C. He, H. G. Yaglioglu, M. Hayvali, A. Elmali and B. Küçüköz, Near - IR Broadband-Absorbing Trans -Bisphosphine Pt(II) Bisacetylide Complexes: Preparation and Study of the Photophysics. *Inorg. Chem.*, 2015, **54**, 7492–7505.
- [S3] J. Wang, Y. Lu, W. McCarthy, R. Conway-Kenny, B. Twamley, J. Zhao and S. M. Draper, Novel Ruthenium and Iridium Complexes of N -Substituted Carbazole as Triplet Photosensitisers. *Chem. Commun.*, 2018, **54**, 1073–1076.
- [S4] S. H. Lim, Y. Su and S. M. Cohen, Supramolecular Tetrahedra of Phosphines and Coinage Metals. *Angew. Chem. Int. Ed.*, 2012, **51**, 5106–5109.
- [S5] M. Sonoda, A. Inaba, K. Itahashi and Y. Tobe, Synthesis of Differentially Substituted Hexaethynylbenzenes Based on Tandem Sonogashira and Negishi Cross-Coupling Reactions. *Org. Lett.*, 2001, **3**, 2419–2421.
- [S6] K. T. Chan, G. S. M. Tong, W.-P. To, C. Yang, L. Du, D. L. Phillips and C.-M. Che, The Interplay between Fluorescence and Phosphorescence with Luminescent Gold(I) and Gold(III) Complexes Bearing Heterocyclic Arylacetylide Ligands. *Chem. Sci.*, 2017, **8**, 2352–2364.
- [S7] Gaussian 09, Revision D.01, M. J. Frisch, G. W. Trucks, H. B. Schlegel, G. E. Scuseria, M. A. Robb, J. R. Cheeseman, G. Scalmani, V. Barone, B. Mennucci, G. A. Petersson, H. Nakatsuji, M. Caricato, X. Li, H. P. Hratchian, A. F. Izmaylov, J. Bloino, G. Zheng, J. L. Sonnenberg, M. Hada, M. Ehara, K. Toyota, R. Fukuda, J. Hasegawa, M. Ishida, T. Nakajima, Y. Honda, O. Kitao, H. Nakai, T. Vreven, J. A. Montgomery, Jr., J. E. Peralta, F. Ogliaro, M. Bearpark, J. J. Heyd, E. Brothers, K. N. Kudin, V. N. Staroverov, T. Keith, R. Kobayashi, J. Normand, K. Raghavachari, A. Rendell, J. C. Burant, S. S. Iyengar, J. Tomasi, M. Cossi, N. Rega, J. M. Millam, M. Klene, J. E. Knox, J. B. Cross, V. Bakken, C. Adamo, J. Jaramillo, R. Gomperts, R. E. Stratmann, O. Yazyev, A. J. Austin, R. Cammi, C. Pomelli, J. W. Ochterski,

- R. L. Martin, K. Morokuma, V. G. Zakrzewski, G. A. Voth, P. Salvador, J. J. Dannenberg, S. Dapprich, A. D. Daniels, O. Farkas, J. B. Foresman, J. V. Ortiz, J. Cioslowski, and D. J. Fox, Gaussian, Inc., Wallingford CT, 2013.
- [S8] T. Lu and F. Chen, Multiwfn: A Multifunctional Wavefunction Analyzer. *J. Comput. Chem.*, 2012, **33**, 580–592.
- [S9] M. Sheik-Bahae, A. A. Said, T.-H. Wei, D. J. Hagan, E. W. Van Stryland, Sensitive Measurement of Optical Nonlinearities Using a Single Beam. *IEEE J. Quantum Electron.* 1990, **26**, 760–769.
- [S10] J. Sun, Z. Liu, C. Yan, X. Sun, Z. Xie, G. Zhang, X. Shao, D. Zhang and S. Zhou, Efficient Construction of Near-Infrared Absorption Donor–Acceptor Copolymers with and without Pt(II)-Incorporation toward Broadband Nonlinear Optical Materials. *ACS Appl. Mater. Interfaces*, 2020, **12**, 2944–2951.
- [S11] Y. Song, J. Sun, X. He, M. Liao, J. Zhao, W. Zeng, S. Zhou and H. Chen, N-Doped Nonalternant Nanoribbons with Excellent Nonlinear Optical Performance. *Angew Chem Int Ed*, 2023, **62**, e202306418.
- [S12] W. Feng, K. Liu, J. Zang, G. Wang, R. Miao, L. Ding, T. Liu, J. Kong and Y. Fang, Flexible and Transparent Oligothiophene-o-Carborane-Containing Hybrid Films for Nonlinear Optical Limiting Based on Efficient Two-Photon Absorption. *ACS Appl. Mater. Interfaces*, 2021, **13**, 28985–28995.